DEGREE PROJECT IN SPACE TECHNOLOGY
SECOND CYCLE, 30 CREDITS
STOCKHOLM, SWEDEN 2016

Attitude Determination and Control of the CubeSat MIST

JIEWEI ZHOU

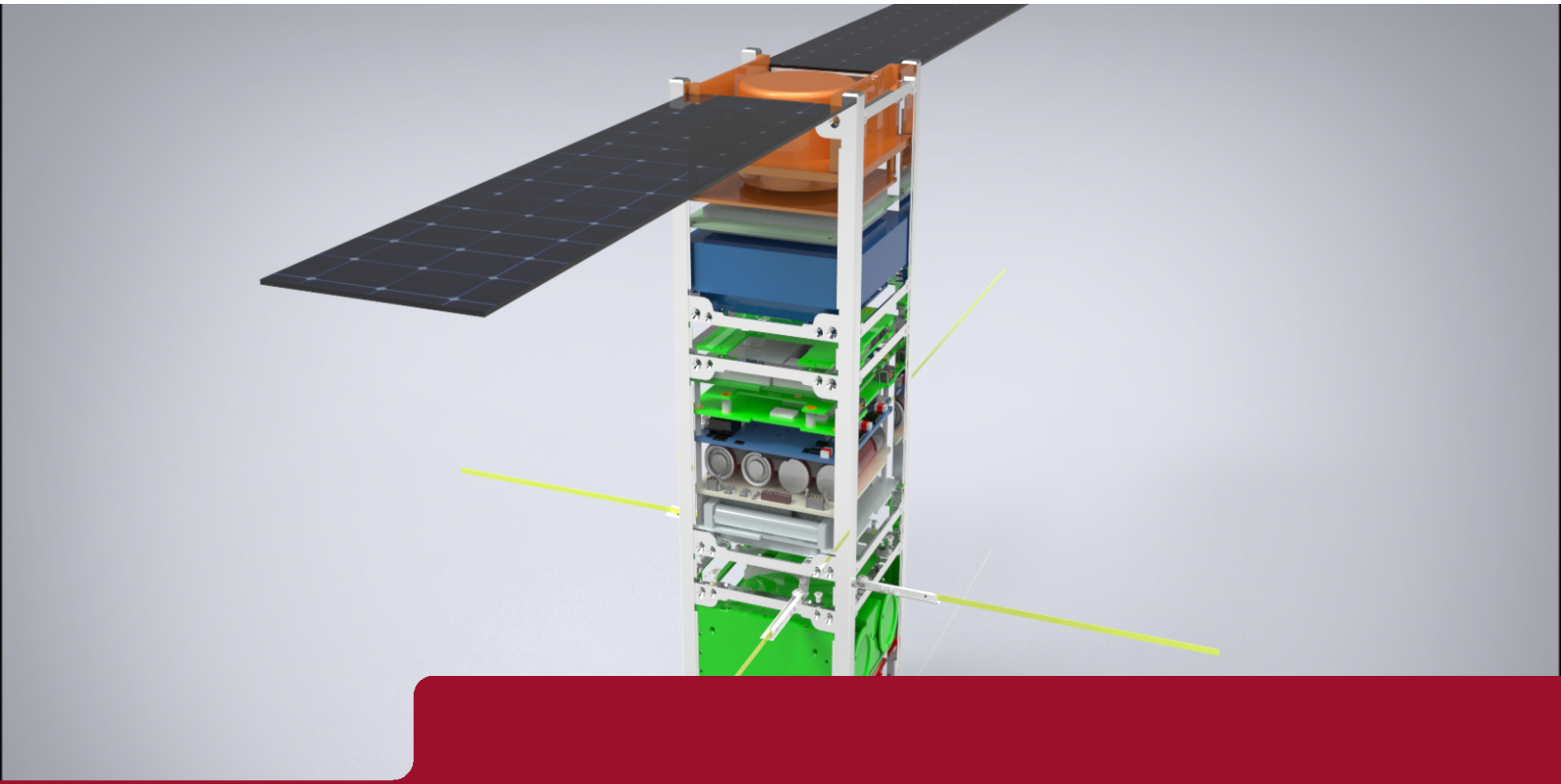

KTH ROYAL INSTITUTE OF TECHNOLOGY
SCHOOL OF ENGINEERING SCIENCES

Preface

The thesis work presented in this paper has been carried out between January and June 2016 under the scheme of the CubeSat Student Satellite Project MIST at KTH. I did it as a member of the 3rd MIST Student Team under the supervision of Dr. Gunnar Tibert, Associate Professor at the Department of Aeronautical and Vehicle Engineering at KTH, and Dr. Sven Grahn, the former Technical Director of the Swedish Space Corporation and the Project Manager of MIST.

I am very thankful to Gunnar and Sven for having offered me this great opportunity to work in a real engineering project and contribute to build a satellite that will be launched in the near future. Many thanks to them also for their valuable guidance during my work, their experience in a large number of real satellite missions definitely helped me learn and make a better thesis.

I would like to thank Prof. Yifang Ban for helping me to get in contact with Gunnar and Sven when I was looking for a thesis work at KTH.

During my everyday work inside the MIST Student Team I was surrounded by great people that are not only quite professional and skillful in their respective fields but very pleasant persons to deal with as well. Many thanks to all of them for their cooperation to my work, specially to the Team Leader Simon Görries, Project Assistant Agnes Gårdebäck and the rest of members working in attitude control Oscar Bylund and Csaba Jéger.

Finally, but certainly not least, I would like to say thanks to my family and friends for supporting me during my work. My very special thanks to Shreyas and Rutvika, who were my most close friends during my Erasmus+ stay in Stockholm.

Jiewei Zhou
Madrid
July, 2016

Abstract

The ADCS concept in MIST reflects the limitations of the CubeSat in terms of space, power and on-board computer computational capability. The control is constrained to the use of only magnetic torquers and the determination to magnetometers and Sun sensors in spite of the the under-actuation and under-determination during eclipses. Usually small satellites with a similar ADCS and demanding requirements fail, therefore MIST would be a design reference for this kind of concept in the case it succeeds.

The objectives of this thesis work are the feasibility assessment of the concept to meet the nominal requirements in MIST and the consideration of alternatives. Firstly, the importance of gravitational stabilization and different configurations for the inertial properties are analyzed based on the linear stability regions for nadir pointing spacecraft. Besides, extended stability regions are derived for the case when a momentum wheel is used to consider alternative options for passive stabilization in terms of the inertial properties. Then a controller based on the Asymptotic Periodic Linear Quadratic Regulation (AP LQR) theory, the currently most extended and effective for pure magnetic control in small satellites, is assessed. Also a Liner Quadratic Regulator design by means of numerical optimization methods, which has not been used in any real mission, is considered and its performances compared with the AP LQR. Regarding attitude determination a Linear Kalman Filter is designed using the AP LQR theory. Finally, a robustness analysis is conducted via Monte Carlo simulations for those control and determination strategies.

Sammanfattning

Systemet för attitydstyrning och -bestämning i nanosatelliten MIST reflekterar små satelliters begränsningarna i utrymme, elkraft och omborddatorkapacitet. Regleringen är begränsad till styrning med magnetspolar som genererar kraftmoment. För attitydbestämningen används magnetometrar och solsensorer trots under-manövrering och -bestämning vid solförmörkelse. Vanligtvis misslyckas små satelliter med liknande reglersystem och höga krav, så om MIST lyckas skulle den bli ett referenskoncept.

Målen med detta examensarbete är att utföra en genomförbarhetsstudie av ett reglerkoncept för att möta de nominella kraven för MIST samt undersöka av alternativa reglersystem. Effekten av gravitationsstabilisering och olika massträghetskonfigurationer har analyserats med hjälp av linjäriserade stabilitetsregioner för en nadirpekande satellit. Stabilitetsregionerna förstoras då ett roterande hjul införs i ett alternativt stabiliseringskoncept eftersom det roterande hjulet påverkar de effektiva massträghetsmomentet. Regleringsalgoritmen som utvärderats i detta arbete är baserad på teorin om Asymptotisk Periodisk Linjär Kvadratisk Regulering (AP LKR), den som är mest använd samt effektiv för ren magnetisk styrning av små satelliter. En utformning av ett koncept baserat på Linjär Kvadratisk Reglering med numerisk optimering, vilket inte tidigare verkar använts för ett riktigt rymduppdrag, har undersökts och jämförts med AP LKR-regleringen. När det gäller attitydbestämningen så har ett linjärt Kalmanfilter utformats för AP LKR-regleringen. Slutligen så har en robusthetsanalys gjorts genom Monte Carlo-simuleringar för styrnings- och bestämningsstrategierna.

Resumen

El concepto para el ADCS en MIST refleja las limitaciones de los CubeSats en cuanto a espacio, potencia y capacidad computacional del ordenador a bordo. El control está restringido al uso de sólo magnetopares y la determinación a magnetómetros y sensores de Sol a pesar de la imposibilidad de actuación según todos los ejes y el conocimiento incompleto en actitud durante eclipses. Normalmente pequeños satélites con un ADCS similar y exigentes requisitos fallan, por la tanto MIST sería una referencia de diseño para este tipo de concepto en el caso de que tenga éxito.

Los objetivos de este trabajo fin de máster son la evaluación de la viabilidad del concepto para cumplir los requisitos nominales en MIST y la consideración de alternativas. Primero, la importancia de la estabilización gravitacional y diferentes configuraciones para las propiedades másicas son analizadas en base a las regiones de estabilidad lineales para vehículos espaciales apuntando según nadir. Además, regiones de estabilidad extendidas son deducidas para el caso en el que una rueda de momento es usada con el fin de considerar opciones alternativas de estabilización pasiva en términos de las propiedades másicas. Después un controlador basado en la teoría del Asymptotic Periodic Linear Quadratic Regulation, el actualmente más extendido y efectivo para control magnético puro en pequeños satélites, es evaluado. También un diseño de LQR por medio de métodos de optimización numérica, el cual no ha sido usado en ninguna misión real, es considerado y sus prestaciones comparadas con el AP LQR. En relación a la determinación de actitud un Linear Kalman Filter es diseñado usando la teoría del AP LQR. Finalmente, un análisis de robustez es llevado a cabo a través de simulaciones de Monte Carlo para esas estrategias de control y determinación.

Contents

1 Introduction **1**
- 1.1 Background . . . 1
- 1.2 Problem Statement . . . 1
- 1.3 Previous Work . . . 2

2 Literature Study **2**

3 Modeling **3**
- 3.1 Generalities . . . 3
- 3.2 Spacecraft . . . 5
- 3.3 Disturbances . . . 6
- 3.4 Actuators . . . 7
- 3.5 Sensors . . . 7

4 ADCS Algorithms **8**
- 4.1 Attitude Control . . . 8
- 4.2 Attitude Determination . . . 8

5 Disturbances Analysis **9**
- 5.1 Aerodynamic Torque . . . 9
- 5.2 Residual Dipole . . . 10

6 Passive Stabilization **10**
- 6.1 Gravity Gradient . . . 10
- 6.2 Momentum Bias . . . 12
- 6.3 Pitch-Orbital Resonance . . . 13

7 ADCS Design **14**
- 7.1 Asymptotic Periodic LQR . . . 14
- 7.2 LQR via Numerical Optimization . . . 15
- 7.3 Asymptotic Periodic LQE . . . 20

8 Conclusions and Discussions **21**

References **22**

1 Introduction

1.1 Background

CubeSats were invented in 1999 as an educational tool. They were conceived to be small and simple enough for university students, and with standard sizes to accommodate them in the rockets. Launches of CubeSats increased significantly in 2013. The number of deployments that year was nearly half of the total until then. Currently not only universities are investing in them but the governments and private companies as well. This interest is due to its low cost, the availability of standardized parts, the increased launch opportunities and its versatility [14, 20].

MIST is the first student satellite at KTH, a 3U CubeSat to be built between during 2015 to 2017 and launched soon after that. The payload consists of 7 technical and scientific experiments. The experiments have been proposed from inside KTH, from two Swedish companies and from the Swedish Institute of Space Physics in Kiruna.

The Attitude Determination and Control System (ADCS) concept of MIST consists of magnetic torquers (MTQs) for control whereas magnetometers (MGMs) and Sun sensors are used for determination. This is not the common practice for small satellites with demanding ADCS requirements and usually fails. The reasons are the under-actuation of pure magnetic control (PMC) and lack of complete attitude information associated to magnetometers during eclipses. Moreover, magnetic cleanliness must be assured and a large effort is required [1, 2, 4, 7, 8, 13, 14, 48, 49, 50].

A momentum wheel (MW) has been proposed for MIST. It would remove the under-actuation problem of PMC and has a higher level of torque that would make the spacecraft dynamics faster. Nevertheless, there are also the following downsides:

- It has a limited angular momentum storage capacity as there is only internal momentum exchange. Because of that momentum dumping with actuators may be needed as well.
- It is prone to failure due to the presence of a moving part.
- It occupies more space and it has a higher power consumption.

Currently, there is not a lot of space left inside the CubeSat and then it is unlikely that this option is considered.

There is also a prototype of a propulsion module that will be tested in MIST from one of the experiments. However, these thrusters will not be used for active attitude control. Their only mission related to pointing is to divert the CubeSat from the nominal attitude (described in Sec. 1.2).

In the case of attitude determination the gyroscopes in the on-board computer could be used to deal with the under-determination during eclipses. However, this proposal has been ruled out to reduce power consumption and simplify the on-board data handling.

To sum up, the ADCS concept in MIST is quite challenging and would provide important design recommendations for small satellites with similar problems in the case it succeeds. It would decrease the cost and power consumption and save space being especially attractive for CubeSats, which are a new revolution in space of increasing interest used for a wide range of applications.

1.2 Problem Statement

The nominal ADCS requirements for MIST are, [23]:

- Nadir pointing with the axis of the minimum moment of inertia along nadir and another body axis parallel to the direction of flight.
- An accuracy of 15 deg for nadir pointing during sunlight.
- An accuracy of 5 deg for attitude determination during sunlight.

The other ADCS requirements, de-tumbling and nadir pointing acquisition, will not be considered in this report.

The main objective of this thesis work is to make an assessment of the ADCS concept's feasibility. Moreover, alternatives are also considered for either the case where it is not possible to meet the requirements with the current concept or when there is still possibility to have complementary ADCS hardware.

Other aim is to compare different attitude control and determination strategies for the current concept. New algorithms will be also explored to see whether there is a possibility to improve the performances obtained with traditional methods.

As to the extension of the work less effort will be put into the study of alternative concepts and those related to determination strategies due to the lack of time.

These objectives will be accomplished by means of literature survey, analytical studies and numerical simulations. The Princeton CubeSat Toolbox is available for simulations. However, as it is the academic version the functionality is limited and it is necessary to write complementary codes.

1.3 Previous Work

During the previous semester de-tumbling analyses, survey for ADCS simulation toolboxes and preliminary attitude control studies for the nominal pointing requirement were conducted.

The preliminary work for nominal pointing conditions consisted of literature survey and numerical simulations where perfect attitude knowledge was assumed. The objective was to make an initial assessment of the ADCS concept's feasibility and evaluate the performances when a MW is considered. The studies conducted in this report will be a continuation of these initial analyses.

2 Literature Study

CubeSats and micro-satellites with a mission profile in terms of ADCS similar to MIST are analyzed. The aim is to know the usual control and determination strategies as well as the achievable performances for PMC and when there is lack of complete attitude information during eclipses. Moreover, slightly different alternatives to MIST's ADCS concept are studied as well.

The basic properties about some of the missions studied are summarized in the Table 2.1. Other satellites have been also analyzed and will be mentioned later on as references as well.

There are two commonly used control algorithms for PMC. One of them is the Linear Quadratic Regulator (LQR) used in Gurwin-Techsat, PRISMA, HokieSat and COMPASS-1 [4, 6, 8, 13]. Other less extended method is the COMPASS controller and it is considered in Gurwin-Techsat and UWE-3 [4, 10]. It is interesting to note that both algorithms were used in Gurwin-Techsat and it was launched in 1998. Then giving that, for example, UWE-3 (2013) and PRISMA (2010) are relatively recent missions it could be concluded that there have not been significant breakthroughs in PMC for nadir pointing since at least 20 years ago.

The COMPASS controller feedbacks the differences in BCF and OCF[1] of both Earth magnetic field and its derivative, which are then used for computing the control magnetic moment. The values in BCF could be obtained directly from MGMs. As to those in OCF precise position knowledge and magnetic field model are enough. Thus, it is possible to achieve nadir pointing using only MTQs and MGMs in principle.

Table 2.1: Missions studied for attitude control.

Feature	Gurwin-Techsat	PRISMA (TANGO)	UWE-3	COMPASS-1
Mass (kg)	48	50	1	1
Size (cm × cm × cm)	45 × 45 × 45	80 × 75 × 32	10 × 10 × 10	10 × 10 × 10
Mean Altitude (km)	810	700	645	635
Orbit Inclination (deg)	98	98	98	98
Control Hardware	3 MTQs 1 MW	3 MTQs	6 MTQs 1 RW	3 MTQs
Control Magnetic Moment (Am^2)	1	2.5	0.05	0.1
Residual Dipole Moment (Am^2)	-	0.1	0.05	-
Determination Hardware	3 MGMs	3 MGMs 6 Sun Sensors 1 Fine Sun Sensor	9 MGMs 3 Gyroscopes 6 Sun Sensors	3 MGMs 5 Sun Sensors

The LQR is based on a linearized model around OCF. It minimizes a cost function that considers control accuracy and effort. For that an optimal feedback matrix is obtained by solving a system of ordinary differential equations. In the case of time-invariant systems the problem is reduced to the Algebraic Riccati Equation (ARE). The problem with PMC for satellites is that the system is time-varying since the magnetic field changes throughout the orbit. However, there are methods to simplify the problem by recovering the ARE:

- A technique is the Asymptotic Periodic LQR used in PRISMA and Gurwin-Techsat. It assumes that the magnetic field is periodic, which is more or less true with the orbital period, and the weight of the control effort in the cost function is large enough. Under these conditions an average of the magnetic field over an orbit can be used for the ARE [11].

- A very similar alternative to the Asymptotic Periodic LQR is used in HokieSat. The difference is that now the control magnetic moment used is assured to be perpendicular to the Earth

[1] The coordinate systems BCF and OCF are explained in Sec. 3.1.

magnetic field by means of a mapping function [9].

The most common estimation method is the Extended Kalman Filter (EKF), which is an version of Kalman filter valid for nonlinear systems. It is used in PRISMA, HokieSat and UWE-2 [6, 8, 49]. Other similar extensions for nonlinear systems are also considered such as Isotropic Kalman Filter (IKF) in UWE-3 and Unscented Kalman Filter (UKF) in SEAM [2, 50].

The Kalman filter minimizes the uncertainty in the estimation of the state vector. It uses a process model to predict and a measurement model to correct the initial estimate. The problem is that those models are supposed to be linear and nearly all practical applications imply nonlinear equations. Both EKF and IKF are based on linearized models. The difference between them it is that IKF assumes the same covariance in all the directions for the state vector simplifying the estimation procedure [48]. On the other hand UKF propagates the mean and covariance through the nonlinear models based on the Unscented Transformation to reduce linearization errors [50]. It is more accurate than EKF and it requires a similar computational effort [51].

In addition to the determination hardware in MIST, UWE-2 and UWE-3 have gyroscopes and SEAM has star trackers. Then, they all have sensors to complement the magnetometers and avoid the lack of complete attitude information during eclipses. From numerical simulations it is known that the estimation error is around 0.2 deg for UWE-3, 30 deg in UWE-2 and 0.02 deg in SEAM [48, 49, 50]. The high performance of SEAM is because of the star trackers. In the case of UWE-3 it should be mentioned that there were some errors not taken into account in the modeling of sensors, thus the actual accuracy is expected to be worse. Regarding in-orbit results it is known that the EKF has been proved reliable for UWE-3 having an accuracy around 5 deg [1]. Besides, SEAM has not been launched yet and there is no published information for UWE-2.

The missions PRISMA and COMPASS-1 have similar ADCS concepts to MIST: PMC and only magnetometers available during eclipses. In the case of PRISMA, simulations showed a nadir pointing accuracy of 5 deg and a estimation error around 2 deg [6]. Afterward in-orbit results indicated a pointing error of 15 deg and an accuracy in the estimation of 3 deg [7]. As to COMPASS-1 it is known from flight results that its ADCS failed due to large errors in the Sun sensors [13].

In spite of having a reaction wheel (RW) UWE-3 was supposed to test several PMC algorithms such as COMPASS for nadir pointing [10]. But finally it ended with a residual magnetic moment which has the same order of magnitude as that for control. This is possibly due to the magnetization of the antennas, made out of stainless steel. Thus the original plan was not able to be conducted [1].

Gurwin-Techsat has only magnetometers and then it is more restrictive than MIST in terms of estimation. Simulations suggested that the LQR and COMPASS can meet the pointing requirements with an accuracy of 8 deg and 1 deg, respectively. However it was necessary a small momentum bias in the case of the COMPASS controller to achieve the stabilization. From flight results it is known that a failure of the LKF (Linear Kalman Filter) used for the LQR, possibly due to magnetic disturbances of the stopped MW, impeded the activation of the controller. For the COMPASS controller, in-orbit results showed a nadir pointing accuracy of 3 deg as long as there is a small momentum bias [4].

Finally the following conclusions should be pointed out:

- A determination concept less restrictive than that in MIST could have a worse performance comparing PRISMA and UWE-3. The possible reason is the high level of magnetic disturbances in UWE-3, which affects the magnetometers. It is likely that with the same magnetic cleanliness the results in UWE-3 would be slightly better.
- Similar ADCS concepts to MIST and slightly different alternatives usually fail with the onboard magnetic disturbances being the main reason.
- One of the few missions analyzed with reported ADCS success is PRISMA. From its flight results it could be inferred that it is possible to meet the ADCS requirements in MIST as long as the magnetic cleanliness is assured.
- The Gurwin-Techsat also succeeded with its COMPASS controller. It has a higher nadir pointing accuracy than PRISMA using only magnetometers for estimation. However, MW was used.

3 Modeling

3.1 Generalities

The coordinate systems that will be considered for the study of attitude control and determination

are:

- Earth-Centered Inertial (ECI) frame.
- Body Coordinate Frame (BCF). The z axis has the minimum moment of inertia and is toward the deployable solar panels. Then the x axis is parallel or perpendicular to the panels with the y axis completing a right handed frame.
- Orbit Coordinate Frame (OCF). The z axis is pointing toward zenith and the y axis is perpendicular to the orbital plane. The x axis completes a right handed frame. Besides, the direction of the y axis is so that the x axis is near the direction of flight.

Under the nominal pointing condition BCF coincides with OCF [22].

Table 3.1 contains the reference conditions necessary for attitude studies. Nearly all the results in this report are obtained according to these values. Nevertheless, some of them are uncertain and could be different in some cases. Those results where other conditions are considered will be pointed out.

The orbital parameters correspond to the Two-Line Element Set (TLE) of the Reference Orbit 1 in [22]. The most doubtful value here is for the altitude and it is possible to end with a lower orbit up to 400 km.

The moments of inertia (I_x, I_y and I_z) are estimated assuming a cuboid with a plate in the top for the deployable solar panels. The mass of the panels are obtained from the specifications [41]. Then regarding the cuboid a mass is supposed according to the typical densities of CubeSats. Furthermore, it has been assumed that the panels are along BCF x axis. As mentioned before there is other configuration with the panels along BCF y axis. In that case the moments of inertia I_x and I_y merely switch their current values.

The values x_G, y_G and z_G represent the position for the center of mass. They are given with respect to a coordinate system with the same orientation as BCF and whose origin is the geometric center of the cuboid above mentioned. Here, it is only an assumption that the center of mass coincides with the that geometric center.

In the part of actuators the parameters correspond to the capabilities of the MTQs and MW. Specific explanations about them can be found in Sec. 3.4. The values are from the specifications of the actuators bought for MIST [38, 40].

Regarding the disturbances the parameters are explained in Sec. 3.3. The residual dipole is obtained as the algebraic sum of the on-board electronic equipment and set in the worst direction: perpendicular to the orbital plane. This assumption is since the orbit is polar and then the Earth magnetic field lines are mainly inside the orbital plane. Studies for increasing residual dipole will be conducted.

Table 3.1: MIST reference conditions.

Element	**Parameter**	**Value**
Orbit	Eccentricity	0.001
	Inclination	97.94 deg
	Mean Altitude	645 km
	Period	97.57 min
Inertial Properties	I_x	$0.037\,\mathrm{kgm}^2$
	I_y	$0.051\,\mathrm{kgm}^2$
	I_z	$0.021\,\mathrm{kgm}^2$
	x_G	0 mm
	y_G	0 mm
	z_G	0 mm
Actuators	$\dot{h}_{wmax}$	0.23 mNm
	h_{wmax}	1.7 mNms
	μ_{Cmax}	$0.2\,\mathrm{Am}^2$
Disturbances	μ_{Dx}	$0\,\mathrm{mAm}^2$
	μ_{Dy}	$5\,\mathrm{mAm}^2$
	μ_{Dz}	$0\,\mathrm{mAm}^2$
	C_D	2.1
	Solar Panel ρ_{Sa}	0.75
	Solar Panel ρ_{Ss}	0.17
	Solar Panel ρ_{Sd}	0.08
	Solar Panel ρ_{St}	0
	Radiator ρ_{Sa}	0.15
	Radiator ρ_{Ss}	0.69
	Radiator ρ_{Sd}	0.16
	Radiator ρ_{St}	0
	ρ_{Ea}	1
	ρ_{Es}	0
	ρ_{Ed}	0
	ρ_{Et}	0
Sensors	$\boldsymbol{\omega}_m$	$55\,\frac{\mathrm{nT}}{\sqrt{\mathrm{Hz}}}$
	$\mathbf{b}_m$	50 nT
	$\mathcal{M}_m$	0.5 %
	$\boldsymbol{\omega}_s$	$0.01\,\frac{1}{\sqrt{\mathrm{Hz}}}$
	$\mathbf{b}_s$	0.015
	$\mathcal{M}_s$	0.5 %

The drag coefficient varies from 2 to 4 as indicated in Sec. 3.3 and the value here is only an initial guess. Higher coefficients will be considered when analyzing the performances.

The optical coefficients for radiation pressure with the subscript S are for Sun and those with E are for Earth. The default values from the Princeton

CubeSat Toolbox are used [27].

Finally there are errors for the sensors (explained in Sec. 3.5). In the case of magnetometers the datasheet is used [39]. Regarding the Sun sensors it is known from the supplier that a reasonable error range is 2 to 6 deg and then the parameters are selected to reproduce that range[2]. These errors depend on the temperature and this usually changes over a relatively broad range during a mission.

3.2 Spacecraft

Complete Model

The CubeSat is modeled as a rigid body with movable parts to take into account the possible addition of a momentum wheel. On the other hand, the variable inertial properties caused by the use of the thrusters will not be modeled. This is since it will oblige to also consider the torque thrusters produce and as it was mentioned in Sec. 1.1 while they are used nadir pointing is not required.

Moreover, it is assumed that the motion of the center of mass is uncoupled with respect to the attitude dynamics. The model SGP4 available in the Princeton CubeSat Toolbox is used to propagate the orbit based on the TLE of the Reference Orbit 1 mentioned in Sec. 3.1. This is the most common model for near-Earth orbits, it takes into account the atmospheric drag and uses low-order Earth gravity [25, 27].

The attitude dynamics of the motion with respect to OCF is given by the angular momentum equation

$$\frac{d\mathbf{H}_G}{dt} = \mathcal{I}\dot{\boldsymbol{\omega}} + \boldsymbol{\omega}\times\mathcal{I}\boldsymbol{\omega} + \boldsymbol{\omega}\times\mathbf{h}_w = \mathbf{T}_I + \mathbf{T}_C + \mathbf{T}_D. \quad (3.1)$$

Here $\mathcal{I}$ is the inertia matrix of the entire spacecraft (including the wheel), $\boldsymbol{\omega}$ the angular velocity of the CubeSat and $\mathbf{h}_w$ the angular momentum of the wheel with respect to the CubeSat.

Regarding the torques in the Eq. 3.1, $\mathbf{T}_I$ is the contribution of the inertial forces and it is

$$\mathbf{T}_I = -\mathcal{I}\dot{\boldsymbol{\Omega}} - \boldsymbol{\Omega}\times\mathcal{I}\boldsymbol{\Omega} + 2\boldsymbol{\omega}\times(I_G\mathcal{U} - \mathcal{I})\,\boldsymbol{\Omega} - \boldsymbol{\Omega}\times\mathbf{h}_w. \quad (3.2)$$

In this expression $\boldsymbol{\Omega}$ is the angular velocity of OCF with respect to ECI frame, $\dot{\boldsymbol{\Omega}}$ its derivative in that frame, I_G the moment of inertia around the center of mass and $\mathcal{U}$ the identity matrix.

The other torques in Eq. 3.1 are disturbances $\mathbf{T}_D$ (described in Sec. 3.3) and control torque $\mathbf{T}_C$ (in Sec. 3.4).

The equation of angular momentum is complemented by the kinematic relations between angular velocity and parameters that defined the attitude. Both 3-2-1 Euler angles and quaternion will be used in these equations.

Linear Model

Apart from the above a linear model is also derived. This will help to get preliminary results with less computational effort and understand better the problems studied.

The linear model is defined considering the following assumptions:

- The equations are linearized around the orbital attitude given by OCF.
- There is no orbital eccentricity e, thus Ω is directly the mean motion Ω_o.
- The only disturbance is gravity gradient.
- The momentum wheel is along the BCF y axis.

Furthermore dimensionless parameters are introduced considering that:

- Time derivatives and angular velocities are nondimensionalized with Ω_o.
- Usual values of the magnetic field B_c in the orbit of the CubeSat and magnetic moment μ_c the actuators are able to provide are used for nondimensionalization.
- The control torque given by the momentum wheel is nondimensionalized with $h_{wyo}\Omega_o$ being h_{wyo} the angular momentum in equilibrium.

Based on those considerations it is obtained the state-space representation

$$\dot{\mathbf{x}} = \mathcal{A}\mathbf{x} + \mathcal{B}\mathbf{u}, \quad (3.3)$$

where the terms represent:

- $\mathbf{x}$ is the state vector containing the dimensionless angular velocity in BCF and 3-2-1 Euler angles.

$$\mathbf{x}^T = \begin{bmatrix} p^\star & q^\star & r^\star & \psi & \theta & \phi \end{bmatrix}. \quad (3.4)$$

- $\mathcal{A}$ is the system matrix. It is expressed via the inertial ratios $\sigma_1 = \frac{I_y - I_z}{I_x}$, $\sigma_2 = \frac{I_z - I_x}{I_y}$ and $\sigma_3 = \frac{I_y - I_x}{I_z}$.

[2] The worst case is 5 to 7 deg when the Earth albedo is not modeled. Nevertheless, here an in-between situation has been assumed.

$$\mathcal{A} = \begin{bmatrix} 0 & 0 & \sigma_1 - 1 + \frac{h_{wyo}}{I_x\Omega_o} & 0 & 0 & -4\sigma_1 - \frac{h_{wyo}}{I_x\Omega_o} \\ 0 & 0 & 0 & 0 & 3\sigma_2 & 0 \\ 1 - \sigma_3 - \frac{h_{wyo}}{I_z\Omega_o} & 0 & 0 & -\sigma_3 - \frac{h_{wyo}}{I_z\Omega_o} & 0 & 0 \\ 0 & 0 & 1 & 0 & 0 & 0 \\ 0 & 1 & 0 & 0 & 0 & 0 \\ 1 & 0 & 0 & 0 & 0 & 0 \end{bmatrix}. \tag{3.5}$$

- $\mathbf{u}$ is the input vector. It comprises the dimensionless control magnetic moment and torque provided by the MW in BCF.

$$\mathbf{u}^T = \begin{bmatrix} \mu_x^\star & \mu_y^\star & \mu_z^\star & \dot{h}_{wy}{}^\star \end{bmatrix}. \tag{3.6}$$

- $\mathcal{B}$ is the input matrix. The Earth magnetic field is in this term and it is in OCF. Its variation over the orbit makes the system time-varying.

$$\mathcal{B} = \frac{B_c\mu_c}{I_y\Omega_o^2} \begin{bmatrix} 0 & \frac{B_z}{B_c}\frac{I_y}{I_x} & -\frac{B_y}{B_c}\frac{I_y}{I_x} & 0 \\ -\frac{B_z}{B_c} & 0 & \frac{B_x}{B_c} & -\frac{h_{wyo}\Omega_o}{B_c\mu_c} \\ \frac{B_y}{B_c}\frac{I_y}{I_z} & -\frac{B_x}{B_c}\frac{I_y}{I_z} & 0 & 0 \\ 0 & 0 & 0 & 0 \\ 0 & 0 & 0 & 0 \\ 0 & 0 & 0 & 0 \end{bmatrix}. \tag{3.7}$$

Similar linear models and their derivations can be found in literature [15, 16, 18, 19].

3.3 Disturbances

Here the models for torques caused by disturbances are described. Usual contributions of gravity gradient, residual dipole, aerodynamic torque and radiation pressure are considered.

Most of the models associated to the disturbances considered are functions already implemented in the Princeton CubeSat Toolbox [21, 27]. The only model that is not in the toolbox is the World Magnetic Model 2015 (WMM 2015) and then the function available in MATLAB is used.

Gravity Gradient

The model considered in this case is the most commonly used. It corresponds to the gravity field of a spherical and homogeneous body. Moreover when computing the torque only the first-order term of a Taylor expansion is considered. This expansion is in terms of $\frac{L_c}{r_G}$, where L_c is a typical length of the CubeSat and r_G is the distance of the center of mass to the Earth.

Based on the assumptions stated above the gravity gradient torque is

$$\mathbf{T}_{GG} = \frac{3\mu_E}{r_G^3}\mathbf{u}_G \times \mathcal{I}\mathbf{u}_G. \tag{3.8}$$

Where μ_E is the gravitational parameter of the Earth and $\mathbf{u}_G$ is the unit vector for the center of mass's position.

In the case the orbital eccentricity is small the gravity gradient torque given by Eq. 3.8 can be simplified as

$$\mathbf{T}_{GG} = 3\Omega_o^2\mathbf{u}_G \times \mathcal{I}\mathbf{u}_G, \tag{3.9}$$

where Ω_o is the mean motion.

Residual Dipole

The magnetic disturbances of the on-board electronics are summarized in a total residual dipole. Then using the general expression for the torque a magnetic dipole produces it is obtained that

$$\mathbf{T}_{RD} = \boldsymbol{\mu}_D \times \mathbf{B}. \tag{3.10}$$

In this equation $\boldsymbol{\mu}_D$ is the residual dipole moment and $\mathbf{B}$ is the Earth magnetic field.

For the Earth magnetic field the WMM 2015 and the tilted dipole model are used. The latter is only for cases where simplifications are required to understand better and quicker the fundamentals of the problems analyzed.

Aerodynamic Torque

This disturbance is due to the interaction between the atmosphere and the spacecraft surface.

At orbital altitudes the density is low enough to have a collisionless flow. Under this assumption the air particles impact the surfaces giving rise to a momentum exchange in the direction of the relative motion, which in turn produces a force in the same direction.

Given flat surfaces the force for the face i is given by

$$\mathbf{F}_{ADi} = \begin{cases} \frac{1}{2}\rho C_D A_i \cos\alpha_i \mathbf{V}_w \|\mathbf{V}_w\| & \text{if } \cos\alpha_i > 0 \\ 0 & \text{if } \cos\alpha_i \leq 0 \end{cases}. \tag{3.11}$$

Where $\mathbf{V}_w$ is the relative velocity of the flow, ρ its density, C_D the drag coefficient and A_i the area of the face i. Besides, $\cos\alpha_i = -\frac{\mathbf{V}_w}{\|\mathbf{V}_w\|} \cdot \mathbf{n}_i$ being $\mathbf{n}_i$ the unit outward normal of surface i.

The condition in $\cos\alpha_i$ is to rule out the faces not being impacted by the incident flow. C_D varies between 2 and 4 depending on the amounts of air particles absorbed and reflected. In the case all the particles are absorbed it is 2 and when they all are reflected it is 4.

As for ρ the model AtmJ70 is used. This model takes into account the solar radiation and the geomagnetic storms providing reasonable predictions.

Once the forces are computed the torque is obtained supposing that the point of application for each face is its geometric center. Denoting $\mathbf{r}_i$ as the position for the geometric center of the face i with respect to the center of mass it is obtained that

$$\mathbf{T}_{AD} = \sum_i \mathbf{r}_i \times \mathbf{F}_{ADi}. \tag{3.12}$$

Radiation Pressure

This disturbance is due to the interaction of the photons emitted by a source and the faces of the spacecraft. A photon striking a surface can be absorbed, specularly reflected, diffusely reflected or transmitted. In relation to the fractions of the incoming photons for a surface it is true that

$$\rho_a + \rho_s + \rho_d + \rho_t = 1, \tag{3.13}$$

where ρ_a is the fraction absorbed, ρ_s specularly reflected, ρ_d diffusely reflected and ρ_t transmitted.

Assuming flat surfaces the force produced in the face i is given by

$$\mathbf{F}_{Ri} = -pA_i\mathbf{s}\cdot\mathbf{n}_i\left[2\left(\rho_s\mathbf{s}\cdot\mathbf{n}_i + \frac{\rho_d}{3}\right)\mathbf{n}_i + (\rho_a+\rho_d)\,\mathbf{s}\right]. \tag{3.14}$$

In this equation $p = \frac{F_p}{c}$ is the radiation pressure being F_p the flux density of the source and c the speed of light. $\mathbf{s}$ is the unit vector for the position of the source with respect to the center of mass

As in the case of the aerodynamic torque here is also the condition in $\mathbf{s}\cdot\mathbf{n}_i = \cos\gamma_i$, that is, when a face is not illuminated by the source ($\cos\gamma_i \leq 0$) there is no force.

Once the force for each surface is computed the torque is obtained as in the case of the aerodynamic torque with

$$\mathbf{T}_R = \sum_i \mathbf{r}_i \times \mathbf{F}_{Ri}. \tag{3.15}$$

The sources considered are the Sun, the Earth albedo and the direct radiation from Earth.

3.4 Actuators

MIST has three single-axis MTQs and a possible MW. There are a lot of details to be added to the ideal models, however only the control limits are considered for now.

The torque provided by the MTQs is the same as that for the residual dipole in Sec. 3.3,

$$\mathbf{T}_{Cm} = \boldsymbol{\mu}_C \times \mathbf{B} \text{ for } \|\boldsymbol{\mu}_C\| \leq \mu_{Cmax}. \tag{3.16}$$

Here $\boldsymbol{\mu}_C$ is the control magnetic moment and μ_{Cmax} is its the saturation value.

As to the MW the control torque is given by

$$\mathbf{T}_{Cw} = -\dot{\mathbf{h}}_w \text{ for } \|\dot{\mathbf{h}}_w\| \leq \dot{h}_{wmax} \text{ and } \|\mathbf{h}_w\| \leq h_{wmax}. \tag{3.17}$$

In this equation $\dot{h}_{wmax}$ and h_{wmax} are the saturation values for the control torque and angular momentum, respectively.

3.5 Sensors

A model for the sensors is obtained based on the work [24] done for MIST and [28] conducted previously for other project. The inaccuracies considered for the sensors are:

- Bias. It is a static offset that could change from one operating cycle to another.
- Noise. This is a random error and it is usually modeled as Gaussian white noise[3].
- Scale factor. This is proportional to the actual value of what is measured and comes from the sensitivity of the sensors, that is, the minimum value they are able to distinguish.
- Crossed-coupling. It is due to errors in the manufacturing and misalignment in the placement of the sensors. Those errors cause that the measurement in one axis is affected proportionally by the other axes.

The mathematical expressions based on the model described above are

$$\tilde{\mathbf{B}} = \mathbf{b}_m + \mathcal{M}_m\mathbf{B} + \boldsymbol{\omega}_m \tag{3.18}$$

for the magnetometers and

$$\tilde{\mathbf{u}}_S = \mathbf{b}_s + \mathcal{M}_s\mathbf{u}_S + \boldsymbol{\omega}_s \tag{3.19}$$

for the Sun sensors. Here the terms in the left-hand side are the measured Earth magnetic field (Eq. 3.18) and Sun vector (Eq. 3.19). In the right-hand side the 1st term is bias, the 2nd represents scale factor and crossed-coupling and the 3rd is noise.

[3] It is a stochastic process where the current instant is uncorrelated with respect to other instants. Thus, it has a constant power spectral density and it is equally important in all the frequencies. Besides, it follows a Gaussian distribution.

4 ADCS Algorithms

4.1 Attitude Control

The LQR computes an input vector for the linear model in Eq. 3.3. This input vector minimizes for any initial condition the cost function given by

$$J = \int_0^T \left(\mathbf{x}^T \mathcal{Q}_c \mathbf{x} + \mathbf{u}^T \mathcal{R}_c \mathbf{u}\right) dt, \tag{4.1}$$

where T is time chosen to evaluate the performance, $\mathcal{Q}_c$ is the weighting matrix for control accuracy and $\mathcal{R}_c$ for control effort.

The general solution of this Calculus of Variations problem is

$$\mathbf{u} = -\mathcal{R}_c^{-1} \mathcal{B}^T \mathcal{P}(t) \mathbf{x}. \tag{4.2}$$

Here $\mathcal{P}(t)$ is an unknown matrix to be determined through a system of ordinary differential equations.

In the case of time-invariant systems $\mathcal{P}$ is constant and the problem is simplified to the ARE as mentioned in Sec. 2 and which is given by

$$\mathcal{P}\mathcal{A} + \mathcal{A}^T P - \mathcal{P}\mathcal{B}\mathcal{R}_c^{-1}\mathcal{B}^T\mathcal{P} + \mathcal{Q}_c = 0. \tag{4.3}$$

However, as seen in Sec. 3.2 the input matrix changes along the orbit and then the system is time-varying. Thus, different approaches with a constant $\mathcal{P}$ are considered in Sec. 7 for a practical design.

Finally it should be mentioned that despite the fact that this controller is the most extended for PMC it can be used for any other actuator.

4.2 Attitude Determination

The attitude determination method that will be implemented in the simulation models is the LKF. It is also known as LQE (Linear Quadratic Estimator) and is not common for small satellites. The only mission found where it was used is Gurwin-Techsat [4].

Adding uncertainties $\mathbf{w}$ to Eq. 3.3 it is obtained a linear stochastic model for the system given by

$$\dot{\mathbf{x}} = \mathcal{A}\mathbf{x} + \mathcal{B}\mathbf{u} + \mathbf{w}. \tag{4.4}$$

The LQE uses it for a replica of the system to estimate the state vector as

$$\dot{\hat{\mathbf{x}}} = \mathcal{A}\hat{\mathbf{x}} + \mathcal{B}\mathbf{u} + \mathcal{L}\left(\mathbf{y} - \hat{\mathbf{y}}\right). \tag{4.5}$$

Here $\hat{\mathbf{x}}$ is the estimated state vector and the 3rd term of the right-hand side is the feedback of the measurements. This feedback is necessary since the uncertainties in Eq. 4.4 make the estimation drift and it is based on a stochastic linear measurement model given by

$$\mathbf{y} = \mathcal{C}\mathbf{x} + \mathbf{v}. \tag{4.6}$$

In Eq. 4.6 the terms represent:

- $\mathbf{y}$ is the output vector and contains the measurements of the magnetometers and Sun sensors minus the Earth magnetic field and Sun vector in OCF, respectively.

$$\mathbf{y}^T = \begin{bmatrix} \Delta B_x & \Delta B_y & \Delta B_z & \Delta u_{Sx} & \Delta u_{Sy} & \Delta u_{Sz} \end{bmatrix}. \tag{4.7}$$

- $\mathcal{C}$ is the output matrix. It comprises the Earth magnetic field and Sun vector in OCF.

$$\mathcal{C} = \begin{bmatrix} 0 & 0 & 0 & B_y & -B_z & 0 \\ 0 & 0 & 0 & -B_x & 0 & B_z \\ 0 & 0 & 0 & 0 & B_x & -B_y \\ 0 & 0 & 0 & u_{Sy} & -u_{S_z} & 0 \\ 0 & 0 & 0 & -u_{Sx} & 0 & u_{Sz} \\ 0 & 0 & 0 & 0 & u_{Sx} & -u_{Sy} \end{bmatrix}. \tag{4.8}$$

- $\mathbf{v}$ represents the errors in the sensors.

Now returning to the feedback term in Eq. 4.5 $\mathcal{L}$ is the gain matrix and

$$\hat{\mathbf{y}} = \mathcal{C}\hat{\mathbf{x}} \tag{4.9}$$

is the estimated output vector.

The uncertainties $\mathbf{w}$ and $\mathbf{v}$ are supposed to be Gaussian white noises in the LQE theory but actually they are quite complex to modeled. Regarding the errors in the sensors there are several components of different nature as discussed in Sec. 3.5. In the case of $\mathbf{w}$ it contains the nonlinear effects and the lack of complete knowledge for the torques acting over the CubeSat. However, it is well-known that the assumption of Gaussian white noise does usually not worsen significantly the performance of the estimator.

The gain matrix $\mathcal{L}$ is computed by minimizing the covariance of the state vector's estimation error being the solution

$$\mathcal{L} = \mathcal{P}_e(t)\mathcal{C}^T\mathcal{R}_e^{-1}. \tag{4.10}$$

Here $\mathcal{P}_e(t)$ is the covariance of the estimation error and R_e is the covariance of the sensors. The only unknown is $\mathcal{P}_e(t)$ and it is necessary to solve a system of ordinary differential equations to obtain this matrix. For time-invariant systems $\mathcal{P}_e$ is constant and it comes from the ARE

$$\mathcal{A}\mathcal{P}_e + P_e\mathcal{A}^T - \mathcal{P}_e\mathcal{C}^T\mathcal{R}_e^{-1}\mathcal{C}\mathcal{P}_e + \mathcal{Q}_e = 0, \tag{4.11}$$

where $\mathcal{Q}_e$ is the covariance of the uncertainties in the system model. The problem is that $\mathcal{C}$ changes over

the orbit and along the year. When comparing LQE and LQR in Sec. 4.1 there are a lot of similarities. This is since there is a duality and it can be used for a practical design of the LQE based on an approach for LQR (discussed in Sec. 7.3).

5 Disturbances Analysis

Here the importance of the different disturbances considered now for MIST is assessed. The study will be not only for the reference conditions but for other conditions as well given the uncertainty of some parameters in Table 3.1.

Table 5.1 summarizes the relevance of the disturbances for the reference conditions. The procedures followed to estimate the aerodynamic torque is in Sec. 5.1 and the residual dipole torque in Sec. 5.2.

In the case of the torque caused by radiation pressure it has an order of magnitude given by

$$T_R \sim p_c A_c L = 0.03\,\mu\text{Nm}, \tag{5.1}$$

where $p_c = 3\,\mu\text{Pa}$ is the usual value of radiation pressure, $A_c = 0.03\,\text{m}^2$ the characteristic area of the CubeSat and $L = 0.3\,\text{m}$ its length.

Table 5.1: Disturbances under reference conditions.

Disturbance	Order of Magnitude (μNm)
Residual Dipole	0.2
Aerodynamic Torque	0.02
Radiation Pressure	0.03

Returning to the linear model described in Sec. 3.2 the term $I_y\Omega_o^2$ in Eq. 3.7 is a characteristic torque associated to the inertia of the CubeSat. It represents the gravity gradient torque as well as the motion. Considering the reference altitude it turns out to be

$$I_y\Omega_o^2 = I_y\frac{\mu_E}{r_G^3} = 0.06\,\mu\text{Nm}. \tag{5.2}$$

This result indicates that the disturbances prevail over the inertia of the CubeSat under the reference conditions. Hence, the open-loop system's motion will be determined by the disturbances rather than by its own properties.

When talking about a closed-loop system the control torque conducts the motion since it will have usually the same order of magnitude as the maximum disturbance torque given by the residual dipole. The MTQs have a saturation value of $0.2\,\text{Am}^2$ according to Table 3.1. Thus, the residual dipole is not a problem.

5.1 Aerodynamic Torque

The order of magnitude of the aerodynamic torque is

$$T_{AD} \sim \rho_c A_c V_c^2 L. \tag{5.3}$$

In this expression ρ_c is the typical value of the atmospheric density, it depends on the altitude and can be obtained from Fig. 5.1. Then

$$V_c = \sqrt{\frac{\mu_E}{r_G}} \tag{5.4}$$

is the velocity of the CubeSat and it is also a function of the altitude.

Assuming that the deployable solar panels are long BCF x axis they are the main contribution. Moreover the torque they produce is along the BCF y axis.

In the case of the reference altitude it is obtained that $\rho_c = 5\cdot10^{-14}\,\text{kg/m}^3$, $V_c = 7\,\text{km/s}$ and therefore

$$T_{AD} \sim 0.02\,\mu\text{Nm}. \tag{5.5}$$

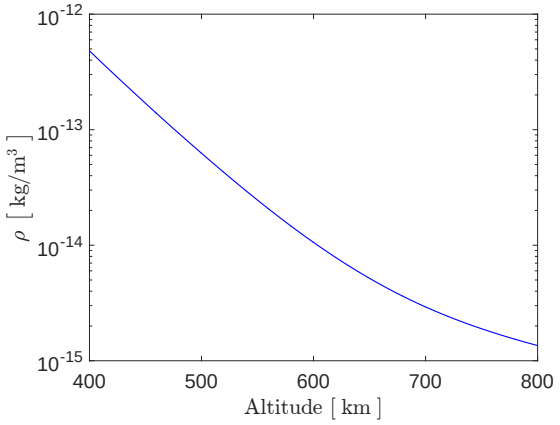

Figure 5.1: Atmospheric density.

As it was mentioned in Sec. 3.1 it is possible to end with an altitude as low as 400 km. Under that condition the velocity of the CubeSat remains with the same order of magnitude after analyzing Eq. 5.4 whereas the density becomes much larger as $\rho_c = 6\cdot10^{-12}\,\text{kg/m}^3$. Hence, the aerodynamic torque also has a huge increase being now

$$T_{AD} \sim 2\,\mu\text{Nm}. \tag{5.6}$$

When MTQs are used the control magnetic moment required is

$$\mu_C \sim \frac{T_{AD}}{B_c} \sim 0.05\,\text{Am}^2, \tag{5.7}$$

which is reasonable given their saturation value.

5.2 Residual Dipole

The Earth magnetic field has an order of magnitude given by

$$B_c \sim B_s \left(\frac{R_E}{r_G}\right)^3, \tag{5.8}$$

where $B_s = 50\,\mu$T is the typical value on the Earth's surface and R_E is the radius of the Earth.

As pointed out before the worst case for MIST is when the residual dipole is normal to the orbital plane. Hence, in that case the torque it generates are along BCF x axis and z axis.

Under the reference conditions $B_c = 40\,\mu$T and the residual dipole torque is

$$T_{RD} \sim B_c \mu_D = 0.2\,\mu\text{Nm}. \tag{5.9}$$

The Earth magnetic field does not change its order of magnitude for an altitude of 400 km according to Eq. 5.8. Thus, the altitude is not a key factor for this disturbance.

The most important parameter here is the residual dipole moment and as indicated before in Sec. 2 it is the main cause of failures in ADCS concepts similar to MIST. Although the estimation now is $5\,\text{mAm}^2$ after adding algebraically the contribution of all onboard electronic devices, there is a large possibility to end with a higher value due to unidentified magnetic effects of some components in the spacecraft. CubeSats such as UWE-3 and SEAM[4] ended with magnetic disturbances of $0.05\,\text{Am}^2$. Given this μ_D the disturbance torque is similar to the case of the aerodynamic torque for an altitude of 400 km.

6 Passive Stabilization

6.1 Gravity Gradient

The environmental torques over the spacecraft corresponding to the gravity gradient and inertial forces could contribute to the stabilization of the attitude around OCF. This type of passive control is called gravitational stabilization and it is a problem that has been analyzed thoroughly in the literature [15, 16, 18, 19].

The stability analysis is based on the linear model derived before in Sec. 3.2. Assuming no momentum bias in the system matrix given by Eq. 3.5 and computing its eigenvalues the conditions for stability are

$$\sigma_1 > \sigma_3, \tag{6.1}$$

$$\sigma_1\sigma_3 > 0 \tag{6.2}$$

and

$$(1 + 3\sigma_1 + \sigma_1\sigma_3)^2 > 16\sigma_1\sigma_3. \tag{6.3}$$

The stability only depends on the inertial ratios σ_1 and σ_3. Thus it is possible to plot the stability regions in the plane σ_1-σ_3 shown in the Fig. 6.1.

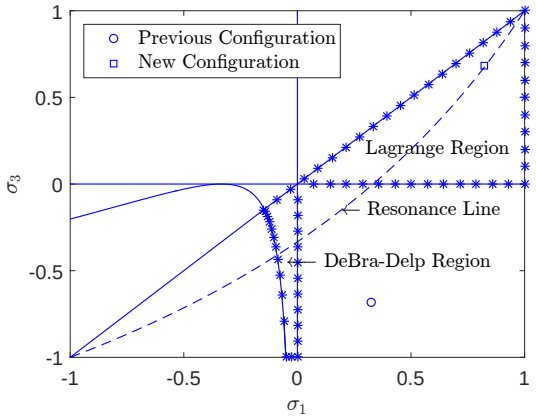

Figure 6.1: Gravity gradient stability regions.

In order to understand better the results in Fig. 6.1 it should be explained the contributions to the stability of the torques involved:

- Gravity gradient. The axis with the minimum moment of inertia needs to be along the local vertical for stability.
- Centrifugal torque. The axis perpendicular to the orbit plane has to have the maximum moment of inertia for stability.
- Coriolis torque. It provides gyroscopic stability irrespective of the inertia matrix.

Furthermore the six possible moments of inertia' orders defined the same number of regions in the σ_1-σ_3 plane as shown in Fig. 6.2. Thus based on this figure it can be concluded that: the Lagrange region is stable due to gravity gradient and centrifugal forces, and the DeBra-Delp region because of the Coriolis forces. The latter is not usually used as the gyroscopic stability disappears when there is energy dissipation in the spacecraft.

[4]The information for UWE-3 is from Table 2.1. As to SEAM it is also a KTH project and there are a lot of data available about it.

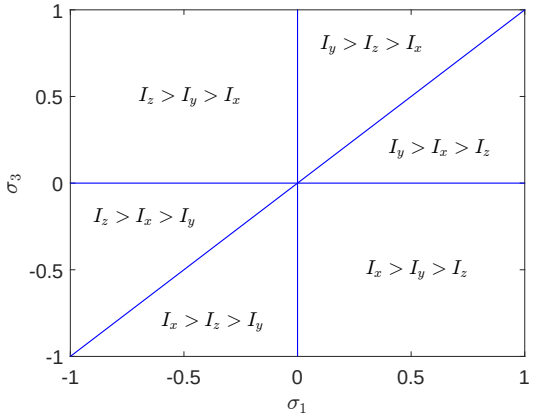

Figure 6.2: σ_1-σ_3 plane.

The configuration of MIST at the end of the last semester was with the deployable solar panels along BCF y axis. This makes it to be in the 4th quadrant of the Fig. 6.1, that is, in a unstable region. In Fig. 6.2 it is seen that the rotation is around the axis with intermediate moment of inertia while the axis with minimum moment of inertia is along the local vertical. Thus, according to what was discussed before the instability in this case is due to centrifugal forces. Fig. 6.3 shows the results in open-loop obtained with a more realistic nonlinear model where similar assumptions are made as in the case of the linear model. It is possible to observe that the instability is in yaw. There are large oscillations around $\psi = -90\,\text{deg}$ as expected since for that orientation MIST is in the stable Lagrange region.

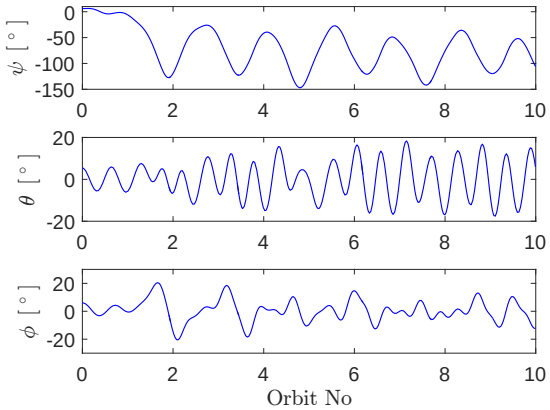

Figure 6.3: Uncontrolled system in old configuration.

In principle, the instability with the panels along BCF y axis could be handled using a controller. However, in the case of PMC it is not possible to always assure stability in the closed-loop system due to the under-actuation. Thus, there are periods of time when the system is basically uncontrolled and they can give rise to significant deviations from OCF if they are long enough. The same simulation as in Fig. 6.3 is run again with a controller now. The results are in Fig. 6.4 and it seems that the pointing error will always become large at some point due to under-actuation.

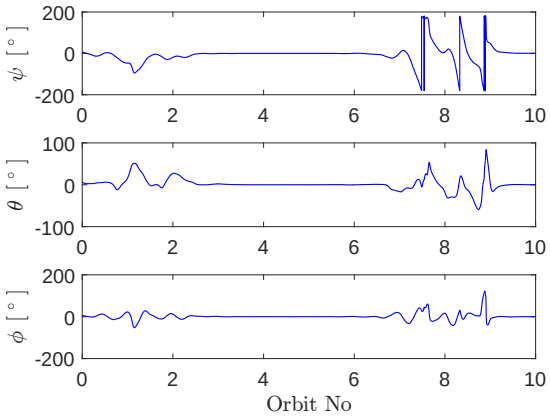

Figure 6.4: Controlled system in old configuration.

The decision then was to rotate the panels and put them along the direction of flight. Now the new configuration is in the stable Lagrange region but near the line associated to a phenomenon known as Pitch-Orbital Resonance as seen in Fig. 6.1. As it will be discussed in Sec. 6.3 this phenomenon can be handled when a controller is used. Therefore, no further modifications are necessary in terms of inertial properties.

Table 6.1: New configuration stability margins.

Parameter	$\boldsymbol{\sigma_1}$	$\boldsymbol{\sigma_3}$	$\boldsymbol{\sigma_1}$-$\boldsymbol{\sigma_3}$
Lower Margin	0.14	0.68	-
Upper Margin	0.18	0.14	-
Margin	-	-	0.10

Table 6.1 contains the stability margins of the new configuration. They represent the allowable variations of the inertial ratios. The columns σ_1 and σ_3 are obtained keeping one of the ratio constant and changing the other one. In the case of σ_1 the lower limit is Eq. 6.1 and the upper limit is actually Eq. 6.16, which is a property of the moments of inertia and not a stability condition. As to σ_3 the lower margin corresponds to Eq. 6.2 and the upper margin to Eq. 6.1. Then the column σ_1-σ_3 is the margin when both ratios are changed at the same time. It

has been computed for the worst case and here that is the displacement that breaches the condition Eq. 6.1.

6.2 Momentum Bias

The previous configuration could be stabilized with a momentum bias along BCF y axis. This is known as dual-spin stabilization. Analyses about this combined with the gravitational stabilization are less common in the literature and will be covered here with some extension. Similar studies can be found in [34] and [35].

The characteristic polynomial of the system matrix given by Eq. 3.5 is

$$\left(\lambda^4 + b\lambda^2 + c\right)\left(\lambda^2 - 3\sigma_2\right) = 0 \tag{6.4}$$

where

$$b = (\sigma_1 + \eta)\left(\sigma_3 + \eta\frac{1-\sigma_3}{1-\sigma_1}\right) + 3\sigma_1 + 1, \tag{6.5}$$

$$c = (4\sigma_1 + \eta)\left(\sigma_3 + \eta\frac{1-\sigma_3}{1-\sigma_1}\right) \tag{6.6}$$

and

$$\eta = \frac{h_{wyo}}{I_x\Omega_o}. \tag{6.7}$$

It should be mentioned that the term $\frac{h_{wyo}}{I_z\Omega_o}$ of the Eq. 3.5 does not appear in these coefficients. This is due to the relations

$$\frac{h_{wyo}}{I_z\Omega_o} = \frac{h_{wyo}}{I_x\Omega_o}\frac{I_x}{I_z} = \eta\frac{I_x}{I_z} \tag{6.8}$$

and

$$\frac{I_x}{I_z} = \frac{1-\sigma_3}{1-\sigma_1}. \tag{6.9}$$

As in the case without momentum bias the eigenvalues $\lambda = \pm\sqrt{3\sigma_2}$ correspond to pitch and it is uncoupled with respect to the motion in the other two angles. This is since the momentum wheel is along BCF y axis and the torque produced is perpendicular to the axis of rotation. Thus, given that the motion in pitch is still independent the condition in Eq. 6.1 or $I_x > I_z$ remains true for stability.

Regarding the other angles the roots of the characteristic polynomial are

$$\lambda^2 = \frac{-b \pm \sqrt{b^2 - 4c}}{2}. \tag{6.10}$$

After the same analysis as in pure gravitational stabilization the conclusion is that for stability λ^2 must be real and negative. Based on this fact the remaining stability conditions are

$$c > 0, \tag{6.11}$$

$$b > 0 \tag{6.12}$$

and

$$b^2 > 4c. \tag{6.13}$$

From the conditions in Eq. 6.1, Eq. 6.11, Eq. 6.12 and Eq. 6.13 it can be concluded that now there is one parameter more affecting the stability: η as well as σ_1 and σ_3. Hence, once a value for η is set it is possible to plot similar stability regions such as in Fig. 6.1.

Before continuing some clarifications should be made about the Lagrange and DeBra-Delp stability regions. The Lagrange region is stabilized by torques that depends on the attitude and not on the angular velocity, thus it is said to be statically stable. The stability in the DeBra-Delp region is due to Coriolis forces and it is said to be statically unstable but gyrically stabilized [15].

Moreover the Lagrange region also turns out to be stable for finite motions when applying the Lyapunov's method. On the other hand, up to now it has not been possible to demonstrate the nonlinear stability or instability for the DeBra-Delp region [34, 36].

Once the above clarifications have been stated the new stability regions are analyzed. The Fig. 6.5 is for a positive value of η. The momentum bias in this case increases the stability contributions of the static torques. Thus, the Lagrange region broadens while the DeBra-Delp area decreases as it is shown in the Fig. 6.5.

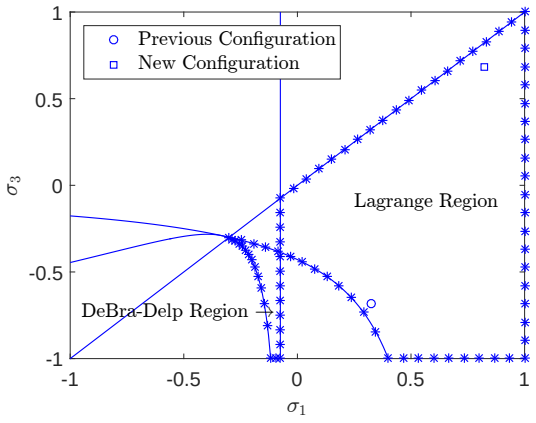

Figure 6.5: Dual-spin stability regions for $\eta = 0.3$.

On the other hand Fig. 6.6 is for a negative value of η. Now the static terms are weakened. That is why the Lagrange area decreases and the DeBra-Delp region grows.

Furthermore under the assumption $\eta \gg 1$ it is

obtained that

$$b \approx \eta^2 \frac{1-\sigma_3}{1-\sigma_1} \tag{6.14}$$

and

$$c \approx \eta^2 \frac{1-\sigma_3}{1-\sigma_1}. \tag{6.15}$$

The conditions in Eq. 6.11 and Eq. 6.12 are verified automatically since it can be demonstrated that

$$|\sigma_1| < 1 \tag{6.16}$$

and

$$|\sigma_3| < 1. \tag{6.17}$$

Then the remaining stability requirement for the motions in yaw and roll gives rise to

$$\frac{1-\sigma_3}{1-\sigma_1} > \frac{4}{\eta^2} \approx 0, \tag{6.18}$$

which is again the condition Eq. 6.1. Therefore, when $\eta \gg 1$ the Lagrange ($\eta \to \infty$) or DeBra-Delp ($\eta \to -\infty$) region occupies the entire lower-right triangle.

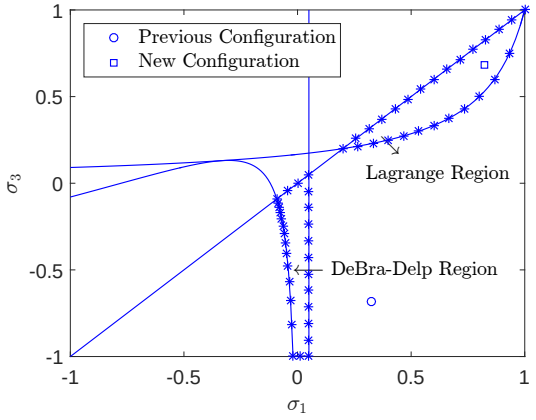

Figure 6.6: Dual-spin stability regions for $\eta = -0.2$.

In the case of MIST, Fig. 6.5 shows that for $\eta = 0.3$ it is already possible to stabilize the previous configuration. However, when using a negative η with a similar magnitude it seems that the CubeSat is still far away from being stable as seen in Fig. 6.6. Then Table 6.2 contains the stability limits for both configurations and it is observed that it is necessary $\eta < -1.29$, which is a order of magnitude larger than the case of a positive momentum bias.

Table 6.2 has as well the column η_{max} corresponding to the maximum angular momentum storage capacity of the MW (taken from Table 3.1). It is seen that it is possible to control the stability in both configurations. Moreover, as it is known η is the ratio between a typical angular momentum the MW can provide and the CubeSat has along the orbit. Hence, the values of η_{max} in both configurations are relatively high and there are a lot of possibilities when modifying the stability regions with the MW in MIST.

Table 6.2: Stability conditions and wheel capability.

Configuration	Conditions	η_{max}
Previous	$\eta > 0.27$ or $\eta < -1.29$	31.06
New	$\eta > -0.38$ or $\eta < -3.30$	42.81

Finally, it should be mentioned that in spite of being able to stabilize with a negative momentum bias this option should not be considered. This is due to the problems of the DeBra-Delp region pointed out before.

6.3 Pitch-Orbital Resonance

The motion in pitch is triggered when there is eccentricity in the orbit. This is since the rotation of the local vertical is not uniform and at the same time the gravity gradient will try that the axis with minimum moment of inertia follows it.

If a small eccentricity is taken into account in the linear model of Sec. 3.2 then an additional term corresponding to the Euler forces will appear in pitch.

In Eq. 3.2 the inertial torque for the Euler forces is

$$\mathbf{T}_E = -\mathcal{I}\dot{\boldsymbol{\Omega}}. \tag{6.19}$$

As mentioned before in Sec. 3.2 $\dot{\boldsymbol{\Omega}}$ is the derivative of the OCF angular velocity in ECI frame. From Kepler's Second Law and the orbit equation $r_G = \frac{h^2/\mu_E}{1+e\cos\nu}$ it is obtained that

$$\Omega = \frac{h}{r_G^2} = \Omega_o \frac{(1+e\cos\nu)^2}{(1-e^2)^{3/2}}, \tag{6.20}$$

where h is the specific angular momentum associated to the orbit and ν the true anomaly. The derivative of Eq. 6.20 in time with respect to ECI frame for $e \ll 1$ is

$$\dot{\Omega} = -2\Omega^2 \frac{e\sin\nu}{1+e\cos\nu} \approx -2\Omega_o^2 e \sin M. \tag{6.21}$$

In Eq. 6.21 the relation between true anomaly ν and mean anomaly M for small eccentricity $\nu = M + 2e\sin M$ was used. Then considering until first-order terms in the Taylor expansion for Eq. 6.19 only the equation of motion in pitch is modified becoming

$$\ddot{\theta} - 3\sigma_2\Omega_o^2\theta = 2\Omega_o^2 e \sin M. \tag{6.22}$$

Similar approaches for studying the Pitch-Orbital Resonance can be found in [15] and [16].

Eq. 6.22 indicates that the additional term has the orbital frequency given that $M = \Omega_o t + M_o$. Hence, there is resonance when the frequency of the system in pitch is equal to the mean motion and that condition is

$$\sigma_2 = -\frac{1}{3}. \tag{6.23}$$

Moreover, it is possible to express σ_2 as

$$\sigma_2 = \frac{\sigma_3 - \sigma_1}{1 - \sigma_1\sigma_3}, \tag{6.24}$$

that is, a function of σ_1 and σ_3. Then taking into account Eq. 6.23 and Eq. 6.24 it is obtained the resonance line in Fig. 6.1.

As pointed out in Sec. 6.1 the new configuration of MIST is near the resonance line. The solution to Eq. 6.22 has a order of magnitude

$$\theta \sim \frac{e}{3\sigma_2 + 1}, \tag{6.25}$$

where it is observed that higher the eccentricity larger the amplitude. MIST has an intended eccentricity of 0.001 (from Table 3.1) and then $\theta \sim 2\,\text{deg}$ for the new configuration. Thus, in principle there is no problem but as mentioned before in Sec. 3.1 the inertia matrix used is just a rough estimation and it is possible that σ_2 is actually even closer to $-\frac{1}{3}$. Furthermore, it is difficult to get such a low eccentricity and analysis must be conducted about this problem.

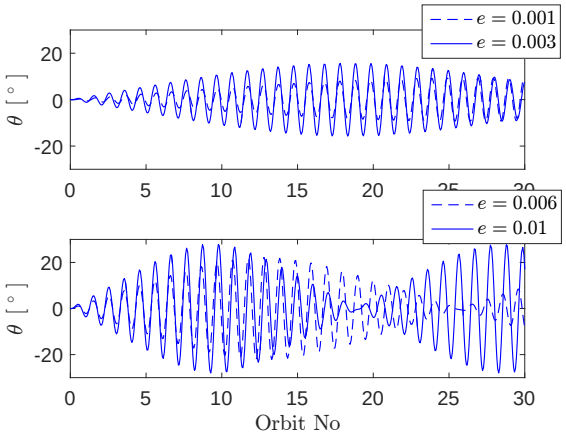

Figure 6.7: Eccentricity in uncontrolled system.

Fig. 6.7 represents the effect of increasing eccentricity in open-loop. These results are obtained from a nonlinear model where the only disturbance considered is the gravity gradient. It is seen that the amplitude begins to be unacceptable around 0.45 rad or 25 deg for a eccentricity of 0.01. In the case of $e = 0.001$ the amplitude is more or less 8 deg. Thus, it has not grown 10 times for $e = 0.01$ as the linear solution would indicate. The nonlinearity decreases its growth rate and the maximum allowable eccentricity is actually smaller than what the linear model would predict.

The same simulations are run again for a controlled system in Fig. 6.8. Here the amplitude is also larger when the eccentricity increases but now it is kept at quite a low value even for $e = 0.02$, which is relatively high for a LEO orbit. Thus, the closed-loop system is able to handle the resonance problem. There are 2 reasons that explain this conclusion:

- The orbit for MIST is polar and then the under-actuation is more or less inside the orbital plane. Hence, it is always possible to generate a torque in the pitch axis with the MTQs and even higher eccentricities than 0.02 are not a problem in principle.

- It takes time to accumulate energy in the system and therefore to have a large pointing error. Fig. 6.7 shows that it is necessary 10 orbits to reach the maximum amplitude for $e = 0.01$. It also seems that higher the eccentricity less time is required. However, simulations suggest that it is still several orbits even for $e = 0.02$. Moreover, if there was an orbit with less inclination the under-actuation in pitch would last only a portion of an orbit. Then the resonance problem can be also mitigated for relatively large eccentricities in more equatorial orbits.

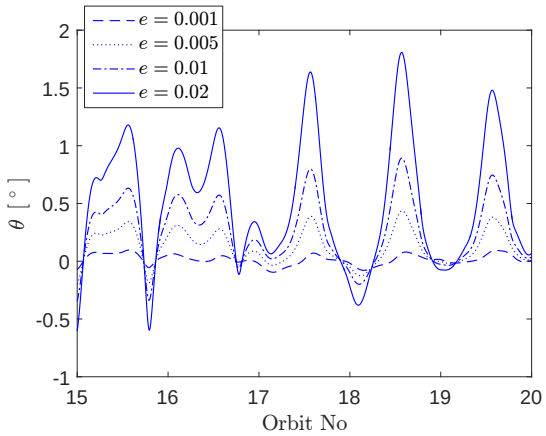

Figure 6.8: Eccentricity in controlled system.

7 ADCS Design

7.1 Asymptotic Periodic LQR

As mentioned in Sec. 2 if the Earth magnetic field is periodic and the weighting matrix for the control

effort $\mathcal{R}_c$ in Eq. 4.1 is large enough the matrix $\mathcal{P}$ from Eq. 4.2 is constant and can be obtained from the average

$$\mathcal{P}\mathcal{A}+\mathcal{A}^T P-\mathcal{P}\frac{1}{T}\int_0^T \left(\mathcal{B}\mathcal{R}_c^{-1}\mathcal{B}^T\right) dt\mathcal{P}+\mathcal{Q}_c = 0, \quad (7.1)$$

where T is taken as the orbital period.

The ARE in Eq. 7.1 can be seen as that associated to the time-invariant system given in closed-loop by

$$\dot{\mathbf{x}} = \frac{1}{T}\int_0^T \left(\mathcal{A} - \mathcal{B}\mathcal{R}_c^{-1}\mathcal{B}^T\mathcal{P}\right) dt\mathbf{x}, \quad (7.2)$$

which is the average over an orbit of the CubeSat's linear model. Moreover, the term between parentheses is the average of the closed-loop system matrix.

In the design of a LQR it is possible to adjust the control accuracy and effort via the matrices $\mathcal{Q}_c$ and $\mathcal{R}_c$, respectively. They need to be defined relatively with respect to each other since the cost function has the same optimum as it multiplied by a constant. Based on the requirements stated in Sec. 1.2 and the limitation of the MTQs in Table 3.1 reasonable choices seem to be

$$\mathcal{Q}_c = \begin{bmatrix} \left(\frac{1}{0.001\,\text{rad/s}}\right)^2\mathcal{U} & 0 \\ 0 & \left(\frac{1}{0.5\,\text{rad}}\right)^2\mathcal{U} \end{bmatrix} \quad (7.3)$$

and

$$\mathcal{R}_c = \left(\frac{1}{0.05\,\text{Am}^2}\right)^2\mathcal{U}. \quad (7.4)$$

These selections have also considered the limited computational capability. Demanding performances imply quick poles in the averaged closed-loop system and high update rates for digital implementation. The maximum update required is given by the estimator since it needs to have poles around 4 times faster than the controller and a reasonable update rate for it is 10 times the velocity of its poles. It is known from the supplier that the MTQs and MGMs can be configured from 1 to 8 Hz. Then the fastest pole with the above $\mathcal{Q}_c$ and $\mathcal{R}_c$ is $0.05\,\frac{1}{\text{s}}$ as seen in Table 7.1. In this case the execution rate of the estimator is around 2 Hz and there is still some margin to the maximum of 8 Hz.

Table 7.1: AP LQR performances.

Performance Index	Value
J	0.0282
J_x	0.0202
J_u	0.0080
$\lvert\lambda\rvert_{max}$	$0.05\,\frac{1}{\text{s}}$

The cost function considered in Table 7.1 corresponds to Eq. 7.5. Regarding J_x and J_u they are the parts associated to control accuracy and effort in Eq. 7.5, respectively. From these results it can be concluded that the performances obtained are around 5 % of the values 0.5 rad and $0.05\,\text{Am}^2$ used for the weighting matrices, that is, 2 deg and $0.003\,\text{Am}^2$ respectively.

7.2 LQR via Numerical Optimization

The matrix $\mathcal{P}$ is obtained by optimizing the cost function directly with a numerical optimization method. It seems that the attitude control feedback in satellites designed in this way has never been implemented in any real mission. Only works at a theoretical level have been found when doing a literature survey and they all claim that it has potential advantages [52, 53, 54].

Here it is possible to consider more factors such as nonlinear effects, other disturbances apart from gravity gradient, estimation errors and so on. Nevertheless, a linear model (in Sec. 3.2) with residual dipole, the most important disturbance as seen in Sec. 5, will be used to have a balance between fidelity and amount of resources available.

The weighting matrices in Eq. 4.1 are assigned the same values as in the case of AP LQR. Furthermore, the integration time is taken as 10 orbits to be representative enough and the objective function is redefined as

$$J = \frac{1}{T}\int_0^T \left(\mathbf{x}^T\mathcal{Q}_c\mathbf{x} + \mathbf{u}^T\mathcal{R}_c\mathbf{u}\right) dt \quad (7.5)$$

to try to have an order of magnitude near one when the desired performance is achieved.

Design of Experiments

Before optimizing it is always recommendable to obtain some properties of the objective function. This stage is called Design of Experiments. Here techniques are used to select representative samples of the design space with the minimum computational effort and to process the information associated to them.

The Latin Hypercube Sampling (LHS) is used to get samples. This method divides each design parameter in N elements with the same length and selects the points so that each of those elements appear once. Thus, the number of chosen points is N as well and each design parameter is evenly sampled [45].

The following details are considered in the sampling:

- In addition to the standard selection criterion of LHS it will be imposed that the distance between the points is maximum. In this way not only all the influence of all the parameters are considered but also it is avoided large regions in the design space without points.

- The solution from AP LQR is used as a reference to rescale the design parameters as

$$\mathcal{P}^{\star}_{ij} = \frac{\mathcal{P}_{ij}}{\mathcal{P}_{APij}}. \tag{7.6}$$

- It is assumed that the solution is near $\mathcal{P}_{AP}$ and then the bounds are defined as

$$5 \geq \mathcal{P}^{\star}_{ij} \geq -5. \tag{7.7}$$

- The number of points is taken as $N = 5000$. This is only a first guess but it seems to be enough to characterize the objective function.

Table 7.2 summarizes the properties of the samples obtained with general statistical parameters. The minimum is lower than what is obtained from $\mathcal{P}_{AP}$ decreasing in a 67 % and then there is possibility to achieve much better performances. The other parameters suggest that there are a large diversity of values and it is confirmed by Table 7.3.

Table 7.2: General statistical parameters.

Parameter	**Value**
Minimum	$9.36 \cdot 10^{-3}$
Maximum	$9.29 \cdot 10^{7}$
Mean	$1.79 \cdot 10^{7}$
Standard Deviation	$1.87 \cdot 10^{7}$

Before explaining the subsequent results in this section some assumptions are made about the objective function:

- There are regions of design space where the system is stable and where it is unstable.

- It is considered that there is stability when

$$J \leq 10 \tag{7.8}$$

as a practical approach.

- Taking $\mathcal{P}_{AP}$ as origin and supposing that it is near the optimum there are directions where the stability increases and where it decreases. In those where it increases the control effort is also larger leading to a higher value of the objective function. As to the other directions at the beginning the system only becomes less stable increasing slightly Eq. 7.5 and at some point it will get unstable with a huge growth in Eq. 7.5.

Analysis over the results in the Table 7.3 indicates that:

- There is only 1.98 % of the points stable while the rest are unstable. Some of them are even toward the unstable directions but the distance to $\mathcal{P}_{AP}$ has not been enough to make the system unstable yet. Thus, there are much more unstable directions than stable directions.

- Only 2.02 % of the samples are in the range $10-10^5$ and then suddenly there are much more points in the range 10^5-10^7. This is due to the outsize increase of the objective function when the system becomes unstable.

Table 7.3: Frequency table.

Range	**Relative Frequency** [%]	**Cumulative Relative Frequency** [%]
$0-10^{-2}$	0.16	0.16
$10^{-2}-10^{-1}$	1.44	1.60
$10^{-1}-1$	0.24	1.84
$1-10$	0.14	1.98
$10-10^{2}$	0.08	2.06
$10^{2}-10^{3}$	0.12	2.18
$10^{3}-10^{4}$	0.22	2.40
$10^{4}-10^{5}$	1.60	4.00
$10^{5}-10^{6}$	8.72	12.72
$10^{6}-10^{7}$	30.22	42.94
$10^{7}-10^{8}$	57.06	100

The derivatives with respect to the design parameters are obtained in Table 7.4. A important result is that the rows 4-6 of $\mathcal{P}$ do not affect the objective function. This can be also deduced from Eq. 4.2 taking into account that $\mathcal{B}$ has zeros in the rows 4-6. Furthermore, the six variables in bold are identified as those that actually influence the objective function due to the following reasons:

- All of them except $\mathcal{P}^{\star}_{r\psi}$ have a derivative higher than 0.5 in magnitude.

- They are the terms that represent the effects of the motion in a certain axis for the same degree of freedom.

- Two sets of nearby directions in the design space toward stable and unstable regions can be found when considering only those terms as it will be explained later on in this section.

Table 7.4: Sensitivity of the design parameters.

Row / Column	p	q	r	ψ	θ	ϕ
p	**−1.86**	0.01	0.03	0.20	0.00	**−1.37**
q	0.10	**−0.52**	0.00	0.10	**1.13**	−0.03
r	0.07	0.01	**−1.67**	**0.13**	0.04	−0.11
ψ	0	0	0	0	0	0
θ	0	0	0	0	0	0
ϕ	0	0	0	0	0	0

Points toward the stable directions and unstable directions among the samples are selected with the criteria

$$J \leq 0.1 \text{ and } D \geq 18 \tag{7.9}$$

and

$$J \geq 10^7, \tag{7.10}$$

respectively. In Eq. 7.9 D is the Frobenius norm of the point with respect to $\mathcal{P}_{AP}$ and its condition is to try to rule out samples in stable regions but toward unstable directions. Due to the conditions considered in Eq. 7.7 the maximum value of D is 30 and 18 is in principle a reasonable limit for the distance.

Then scalar products are taken between:

- Stable directions.
- Unstable directions.
- Stable and unstable directions.

All the directions are given by the unit vectors from the $\mathcal{P}_{AP}$ to the points. Moreover, the scalar products between the same vector are not considered as instances to be studied.

Fig. 7.1 represent the fractions of instances higher than a certain value of the dot product for each case above. In principle the stable directions should be close with respect to each other and the same for the unstable directions. Moreover, both set of directions should be mainly opposite to each other. However, the fractions of scalar products higher than 0.5 are less than 20 % for either stable and unstable cases. Furthermore, the line associated to the mixed dot products between the two sets of points is nearly the same as the line for unstable directions. This result is since all the variables in the rows 1-3 of $\mathcal{P}$ have been considered and there are several irrelevant design parameters.

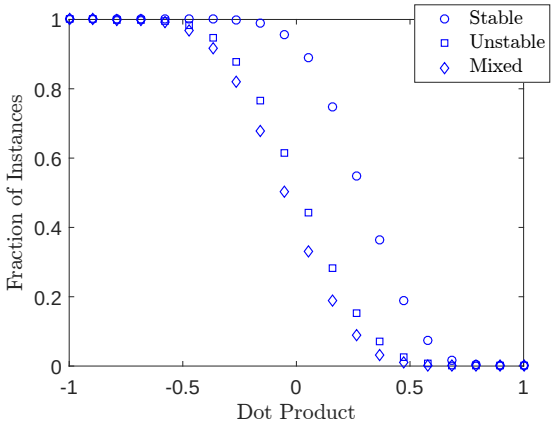

Figure 7.1: Directions.

Fig. 7.2 contains the same but taking into account only the six important variables mentioned before. Now it is clear the nearness for each set of directions and that they tend to be opposite to each other. It should be also pointed out that there is more variability for unstable directions and this is since this type of directions is much larger in number. These results contribute to confirm that the design parameters of Table 7.4 in bold are those really important for the objective function. Furthermore, the assumption made before about the existence of stable and unstable directions seems to be correct[5] considering their respective nearness and that the points selected have very different D.

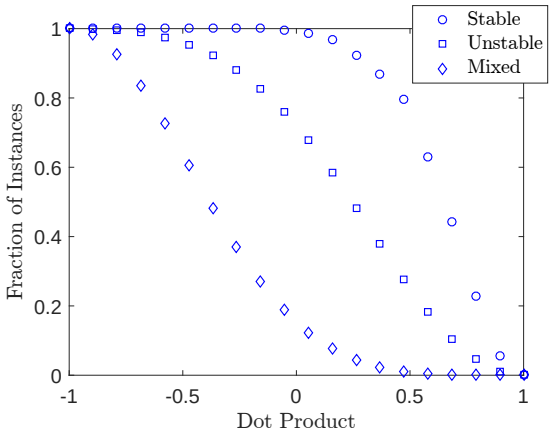

Figure 7.2: Directions with the key variables.

[5]It should be reminded that this assumption is always considering the bounds defined before for $\mathcal{P}^\star$. Otherwise, it is possible that there are problems in the stable directions when breaching those constraints due to the limitation of the MTQs.

Optimization

The optimization is conducted using the following methods:

- Sequential Quadratic Programming (SQP). It combines quadratic approximations and quasi-Newton algorithms. Thus, it is gradient-based and a local method [44, 45].
- Nelder-Mead. This method computes a n-dimensional analogue of a triangle, that is, a geometrical figure enclosed within $n + 1$ vertexes in a n-dimensional space. This is called simplex and it is updated in each iteration by substituting the worst vertex by a nearby point with a lower value of objective function. Hence, it is a local derivative-free algorithm [44, 45].
- Genetic Algorithms (GAs). These are stochastic methods that mimic the evolution process to find the optimum. It takes a set of points in the design space as a population of individuals and measures their suitability to a environment given by the objective function. They are global and derivative-free algorithms [45, 46].

Some considerations are taken into account when optimizing Eq. 7.5:

- The conditions in Eq. 7.7 are used to keep the velocity of the poles so that similar update rates as for the AP LQR are obtained.
- Only the key variables are used for SQP. The other variables would make the Hessian matrix of the quasi-Newton method nearly singular.

The results in Table 7.5 are without elaborate starting points. In the GA the initial population is generated randomly and a vector of zeros is used for Nelder-Mead and SQP. The best solution has been obtained by the GA and the worst by SQP.

Table 7.5: Results without guidance.

Method	**Total Iter.**	**Eval.**	J	J_x	J_u
GA	105	2120	0.0089	0.0007	0.0082
Simplex	682	1040	0.0138	0.0057	0.0081
SQP	52	982	0.0268	0.0186	0.0082

The Earth magnetic field of the simulation model is obtained by interpolation and this causes errors when computing the derivatives numerically. Thus, a larger number of points for interpolation and a lower relative tolerance for integration have been used the case of SQP. Despite that SQP stopped since the step size was smaller than the tolerance value and without meeting the criteria corresponding to optimization problems solved by gradient-based methods. This means that it was not enough and a better solution would have been to implement the Earth magnetic model directly. Furthermore, the time needed to run a simulation for SQP was around the triple for SQP and its actual number of function evaluations would be even larger than in the case of the GA.

Table 7.6: Results with guidance.

Method	**Total Iter.**	**Eval.**	J	J_x	J_u
GA	79	1600	0.0088	0.0007	0.0081
Simplex	269	531	0.0090	0.0009	0.0081
SQP	12	484	0.0094	0.0011	0.0083

Table 7.6 contains the optimization results with good initial approximations now. Points from the conditions Eq. 7.9 are used as initial population of the GA and the solution by AP LQR is considered for Nelder-Mead and SQP. Now, all the results are very similar being that by the GA still the best and that by SQP still the worst. The GA has obtained nearly the same solution as without guidance.

Regarding the computational effort the GA still has the most function evaluations and now SQP is nearly similar to it taking into account what was mentioned above. The number of function evaluations is now smaller than the case without guidance decreasing around 50 % for Nelder-Mead and SQP and 25 % in the case of the GA.

Table 7.7: Standard deviation of the solutions.

Row / Column	p	q	r	ψ	θ	ϕ
p	**0.33**	4.21	1.65	2.74	3.54	**0.22**
q	1.74	**0.80**	3.45	1.30	**0.25**	1.83
r	0.23	4.41	**0.15**	**0.79**	5.05	4.00

The solution by the GA with guidance has only reduced the minimum obtained in the Design of Experiments by 6 %. It means that it was possible to find the solution with a number of samples that has the same order of magnitude as the function evaluations needed for optimization. Therefore, it suggests that good optimization methods for the objective function are those able to explore different regions in design space.

As conclusion, the GA is the best optimization method for this kind of problems. It is more suitable than Nelder-Mead since it is a global method. When comparing with SQP it is not necessary to identity the key variables.

Table 7.4 shows the variability of the different $\mathcal{P}^\star$ obtained. It is again clear that the key variables identified before are those that mainly affect the cost function since they all have a standard deviation smaller than 0.8. Moreover, the results in Table 7.8 seem to indicate that the exact solution of the problem for the key variables is in the boundary defined by Eq. 7.7.

Table 7.8: Mean of the solutions.

Row / Column	p	q	r	ψ	θ	ϕ
p	4.64	-	-	-	-	4.78
q	-	3.59	-	-	2.73	-
r	-	-	4.76	4.08	-	-

Fig. 7.3 represents the fraction of dot products between the solution by the GA with guidance and the points obtained under the conditions Eq. 7.9 higher than a certain value. It is seen that the solution is close to those stable directions as expected. Moreover, as the solutions by the other methods are similar to the GA this result can be extended to them as well.

Finally, it should be mentioned that the LQR designed via numerical optimization is stable when considering the averaged close-loop system introduced for the AP LQR. Moreover, the solution here is not a symmetric matrix as in the case of AP LQR.

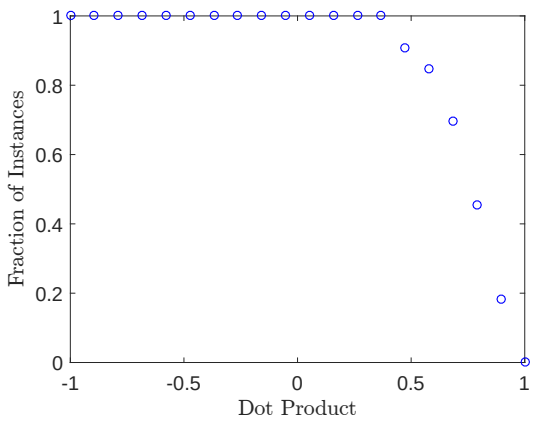

Figure 7.3: GA LQR versus stable directions.

Robustness Analysis

The robustness of the AP LQR and Genetic Algorithm LQR are assessed via Monte Carlo simulations. Random values are obtained using uniform distributions for the following parameters:

- Mean altitude and orbital inclination. They are modified within a $\pm 3\,\%$ with respect to the reference conditions.
- Right ascension of the ascending node and argument of perigee. Here the ranges are between 0 and 2π rad.
- Inertial matrix. The elements in the diagonal are modified within a $\pm 2\,\%$ while the products of inertia in a range defined by the $\pm 2\,\%$ of $\frac{I_x+I_y+I_z}{3}$.
- Residual dipole. It varies from the reference condition until the double of that value.
- Drag coefficient. It changes in its natural range, that is, between 2 and 4.
- Center of mass's position. In each direction a maximum displacement of 10 mm is allowed.

Two simulation models are considered for this study. Both takes into account all the disturbances but one of them supposes perfect attitude knowledge while the other uses estimator explained in Sec. 7.3. For each case two sets of Monte Carlo simulations are obtained with a number of samples $N_m = 100$.

Table 7.9: Percentage of stable instances without estimation errors.

	First Execution	**Second Execution**
AP LQR	79 %	82 %
GA LQR	92 %	98 %

Table 7.9 contains the results without estimation errors. The percentage of simulations that met the stability criterion given by Eq. 7.8 is used to measure the robustness. In both executions of the Monte Carlo simulations the values obtained are consistent and this indicates that the N_m chosen was enough. The conclusion is that both controllers are reasonably robust being the GA LQR a 15 % better on average.

Table 7.10: Percentage of stable instances with estimation errors.

	First Execution	Second Execution
AP LQR	80 %	72 %
GA LQR	86 %	90 %

The results with estimation errors are in Table 7.10. In this case the N_m chosen was also enough. Both controllers are slightly less robust than before. Moreover, GA LQR is 12 % better on average now.

7.3 Asymptotic Periodic LQE

As seen in Sec. 4.2, the LQE has the same problem as the LQR. In principle it is also necessary to solve ordinary differential equations to get the solution $\mathcal{P}_e(t)$. However, it was mentioned that there is a duality between LQE and LQR. Thus, it is possible to consider the AP LQR theory for the estimation problem.

Now $\mathcal{C}$ is the equivalent to $\mathcal{B}$ and it needs to be periodic with the orbital period. The Earth magnetic field can be supposed periodic as seen before. The Sun vector in OCF changes over a year but as the orbit in MIST is Sun-synchronous it could be supposed periodic. Hence, there are enough arguments to apply the AP LQR theory for the LQE design.

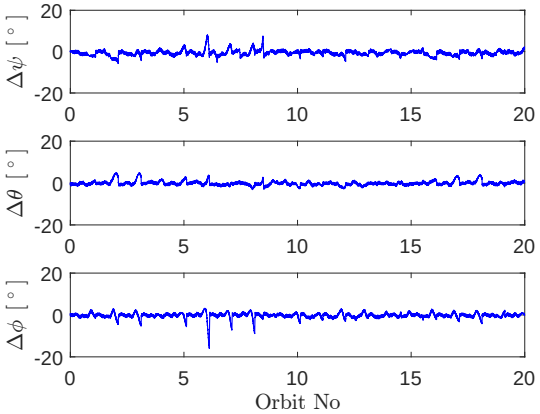

Figure 7.4: Estimation errors.

Fig. 7.4 represents the performance of the AP LQE. It is seen that there are peaks in each orbit. They correspond to eclipses when the Sun sensors are not available and there is under-determination using magnetometers only. Also it seems that the errors in yaw and roll are larger than in pitch. This is since the orbit is polar and the under-determination is mainly inside the orbital plane.

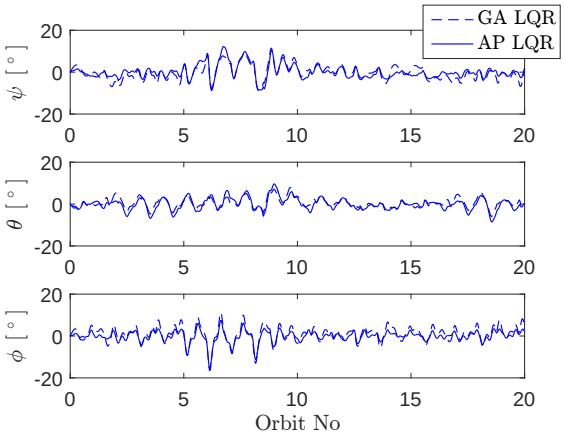

Figure 7.5: Pointing errors.

The pointing error using AP LQR and GA LQR combined with the AP LQR are represented in Fig. 7.5. Again the accuracy in yaw and roll are worse since the orbit is polar and the under-actuation of MTQs does not affect a lot the motion in pitch.

Table 7.11: Performance under sunlight.

	ψ (deg)	θ (deg)	ϕ (deg)	$\Delta\psi$ (deg)	$\Delta\theta$ (deg)	$\Delta\phi$ (deg)
AP LQR	3.34	2.16	3.76	1.04	0.59	0.68
GA LQR	2.90	2.60	2.79	0.99	0.59	0.68

Table 7.11 and Table 7.12 summarize the performance in terms of the Root Mean Square (RMS). It is possible to see that the estimation errors are nearly the same for AP LQR and GA LQR. As to pointing error the GA LQR is slightly worse in pitch but better in roll. Taking into account all the angles GA LQR is more accurate than AP LQR.

Table 7.12: Performance during eclipses.

	ψ (deg)	θ (deg)	ϕ (deg)	$\Delta\psi$ (deg)	$\Delta\theta$ (deg)	$\Delta\phi$ (deg)
AP LQR	3.99	2.84	3.94	1.86	1.54	2.03
GA LQR	4.02	3.24	2.53	1.85	1.59	2.30

The requirements stated in Sec. 7.5 are taken as the RMS when considering all the angles. If the norm of a vector containing all the angles is used the maximum errors allowed under sunlight for each angle are 8.66 deg for pointing and 2.89 deg for estimation. Based on the results from Table 7.11 the conclusion

is that it is possible to meet the ADCS requirements with the ADCS concept in MIST under the reference conditions.

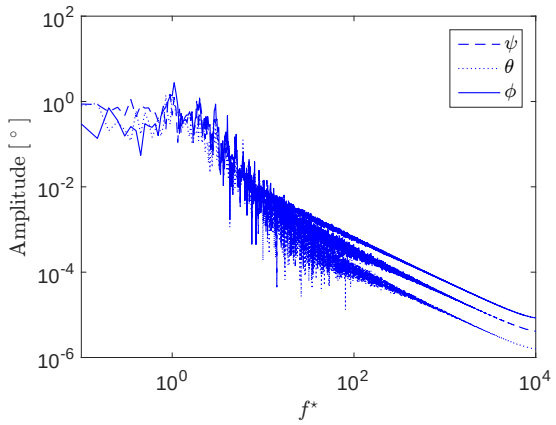

Figure 7.6: Pointing errors in the frequency domain.

Fig. 7.6 represents the pointing error in the frequency domain. A nondimensionalized frequency $f^\star$ is defined with the mean motion Ω_o. As expected the maximum amplitude is around the orbital frequency. Moreover, the amplitude decreases for high frequencies.

8 Conclusions and Discussions

The following points should be remarked in this final part of the report:

- Identical ADCS concepts to MIST usually fail with the on-board magnetic disturbances being the main reason.
- PRISMA is the only small satellite with the same ADCS concept as MIST found that succeeded.
- It is necessary to assure gravitational stabilization for PMC. The under-actuation could make the closed-loop system unstable. In MIST the orientation of the deployable solar panels was changed to have this kind of passive stabilization.
- An alternative solution to the rotation of the solar panels is to provide a momentum bias perpendicular to the orbital plane with a MW. In this case it should be in the direction of the orbital rotation to make the CubeSat be in the Lagrange region. The nonlinear stability for the DeBra-Delp region has not been proved and it disappears when there is energy dissipation.
- The new configuration of MIST is near the Pitch-Orbital Resonance. However, the closed-loop system can handle this problem since the orbit is polar and the under-actuation is inside the orbital plane.
- An LQR designed via numerical optimization could improve the pointing accuracy as well as the robustness of the traditionally used AP LQR. Simulations results indicate that these advantages are more noticeable while the estimation errors are small. However, this could be since the estimator has not been uncoupled from the controller in the simulation models causing a higher noise in the system then.
- It seems that an optimization method able to explore different regions of the design space and derivative-free is the most suitable for an LQR. There is a large number of variables that do not affect the objective function and it is necessary to identify them if a quasi-Newton method is used. Otherwise the Hessian matrix becomes singular.
- The simulation results suggest that the ADCS concept in MIST can meet its requirements under its reference conditions.
- The analyses for different conditions in Sec. 5 are supposing perfect attitude knowledge. When taking into account large estimation errors they could be not valid.

References

[1] S. Busch, P. Bangert, S. Dombrovski, K. Schilling: UWE-3, In-Orbit Performance and Lessons Learned of a Modular and Flexible Satellite Bus for Future Pico-Satellite Formations. In: Proceedings in 65th IAC Congress, IAC-14-B4.6B.6, Toronto, Canada, 2014.

[2] F. Reichel, S. Busch, P. Bangert, K. Ravandoor, K. Schilling: The Attitude Determination and Control System of the Picosatellite UWE-3. In: Proceedings in 19th IFAC Symposium on Automatic Control in Aerospace, Würzburg, Germany, 2013.

[3] M. Yu. Ovchinnikov, D. S. Roldugin, V. I. Penkov: Three-Axis Active Magnetic Attitude Control Asymptotical Study. In: Acta Astronautica 110, 2015, p. 279-286.

[4] M. Guelman, R. Waller, A. Shiryaev, M. Psiaki: Design and Testing of Magnetic Controllers for Satellite Stabilization. In: Acta Astronautica 56, 2005, p. 231-239.

[5] M. Guelman, F. Ortenberg, A. Shiryaev, R. Waler: Gurwin-Techsat, Still Alive and Operational after Nine Years in Orbit. In: Acta Astronautica 65, 2009, p. 157-164.

[6] C. Chasset, S. Berge, P. Bodin, B. Jakobsson: 3-Axis Magnetic Control with Multiple Attitude Profile Capabilities in the PRISMA Mission. In: Proceedings in 57th IAC Congress, IAC-06-C1.2.3, Valencia, Spain, 2006.

[7] C. Chasset, R. Noteborn, R. Larsson, P. Bodin, B. Jakobsson: 3-Axis Magnetic Control, Flight Results of the TANGO Satellite in the PRISMA Mission. In: CEAS Space Journal 5.1-2, 2013, p. 1-17.

[8] K. L. Makovec, A. J. Turner, C. D. Hall: Design and Implementation of a Nanosatellite Attitude Determination and Control System. In: Proceedings in the 2001 AAS/AIAA Astrodynamics Specialists Conference, AAS 01-311, Quebec City, Canada, 2001.

[9] K. L. Makovec: A Nonlinear Magnetic Controller for Three-Axis Stability of Nanosatellites. Master Thesis, Virginia Polytechnic Institute and State University, Blacksburg, USA, 2001.

[10] F. Reichel: Attitude Control System of UWE-3. Master Thesis, Julius Maximilians University of Würzburg, Würzburg, Germany, 2012.

[11] M. L. Psiaki: Magnetic Torquer Attitude Control via Asymptotic Periodic Linear Quadratic Regulation. In: Journal of Guidance, Control and Dynamics 24.2, 2001, p. 386-394.

[12] A. Aydinlioglu, M. Hammer: COMPASS-1 Picosatellite, Magnetic Coils for Attitude Control. In: Proceedings in 2nd International Conference on Recent Advances in Space Technologies, Istanbul, Turkey, 2005.

[13] A. Scholz, F. König, S. Fröhlich, J. Piepenbrock: Flight Results of the COMPASS-1 Mission. In: Acta Astronautica 67.9-10, 2010, p. 1289-1298.

[14] Satellite Missions Database. Last Checked: 11/02/2016. https://directory.eoportal.org/web/eoportal/satellite-missions.

[15] P. C. Hughes: Spacecraft Attitude Dynamics. Dover Publications, 2004.

[16] J. R. Wertz: Spacecraft Attitude Determination and Control. Kluwer Academic Publishers, 1978.

[17] F. L. Markley, J. L. Crassidis: Fundamentals of Spacecraft Attitude Determination and Control. Springer, 2014.

[18] M. J. Sidi: Spacecraft Dynamics and Control, a Practical Engineering Approach. Cambridge University Press, 1997.

[19] H. Schaub, J. L. Junkins: Analytical Mechanics of Space Systems. American Institute of Aeronautics and Astronautics, 2009.

[20] N. Jones: Mini Satellites Prove their Scientific Power. In: Nature 508, 2014, p. 300-301.

[21] M. Paluszek, P. Bhatta, P. Griesemer, J. Mueller, S. Thomas: Spacecraft Attitude and Orbit Control. Princeton Satellite Systems, 2009.

[22] S. Grahn: MIST Reference Orbit. MIST Project Document, KTH, Stockholm, Sweden, 2015.

[23] S. Grahn: MIST Technical Requirements for Subsystem Procurement. MIST Project Document, KTH, Stockholm, Sweden, 2015.

[24] C. Jéger: ADCS Sensors and Actuators Modeling. MIST Project Document, KTH, Stockholm, Sweden, 2016.

[25] F. R. Hoots, R. L. Roehrich: Models for Propagation of NORAD Element Sets. Project Space Track Report No. 3, Aerospace Defense Command, Peterson AFB, Colorado Springs, USA, 1988.

[26] Definition of TLE Coordinate System. Last Checked: 01/04/2016. http://spaceflight.nasa.gov/realdata/sightings/SSapplications/Post/JavaSSOP/SSOP_Help/tle_def.html.

[27] Princeton CubeSat Toolbox. Codes Description, Princeton Satellite Systems, Plainsboro, USA, 2015.

[28] J. Zhou: Sensor Data Fusion for an AHRS. Bachelor Thesis, Technical University of Madrid, Madrid, Spain, 2014.

[29] J. Peláez Álvarez: Passive Stabilization of Satellites. Astrodynamics and Attitude Dynamics Course Notes, Technical University of Madrid, Madrid, Spain, 2015.

[30] G. Tibert: Nonlinear Control. Spacecraft Dynamics Course Notes, KTH, Stockholm, Sweden, 2015.

[31] M. L. Ni: Existence Condition on Solutions to the Algebraic Riccati Equation. In: Acta Automatica Sinica 34.1, 2008, p. 85-87.

[32] W. F. Arnold, A. J. Laub: Generalized Eigenproblem Algorithms and Software for Algebraic Riccati Equations. In: Proceedings of the IEEE 72.12, 1984, p. 1746-1754.

[33] B. D. O. Anderson, J. B. Moore: Linear Optimal Control. Prentice Hall, 1971.

[34] R. Longman, P. Hagedorn, A. Beck: Stabilization due to Gyroscopic Coupling in Dual-Spin Satellites Subject to Gravitational Torques. In: Celestial Mechanics 25.4, 1981, p. 353-373.

[35] M. R. M. Crespo da Silva: Attitude Stability of a Gravity-Stabilized Gyrostat Satellite. In: Celestial Mechanics 2.2, 1970, p. 147-165.

[36] M. T. Aygün, U. Daybelge: Attitude Stability of DeBra-Delp Satellites in Circular Orbit. In: Journal of Guidance, Control and Dynamics 21.6, 1998, p. 965-970.

[37] D. Brundin: MIST Project Handbook. MIST Project Document, KTH, Stockholm, Sweden, 2015.

[38] CubeWheel Datasheet. Last Checked: 22/04/2016. http://www.isispace.nl/brochures/CubeWheel_BrochureCubeSpace.pdf.

[39] XEN1210 Magnetic Sensor Datasheet. Last Checked: 22/04/2016. http://www.compotrade.ru/Components/Sensixs/XEN1210.pdf.

[40] ISIS Magnetorquer Board. Last Checked: 22/04/2016. http://www.cubesatshop.com/index.php?option=com_virtuemart&Itemid=69&vmcchk=1&Itemid=69.

[41] ISIS CubeSat Solar Panels. Last Checked: 02/06/2016. http://www.cubesatshop.com/index.php?option=com_virtuemart&Itemid=79.

[42] World Magnetic Model 2015. Last Checked: 22/04/2016. http://www.ngdc.noaa.gov/geomag/WMM/.

[43] P. Y. Papalambros, D. J. Wilde: Principles of Optimal Design, Modeling and Computation. Cambridge University Press, 2003.

[44] J. Nocedal, S. J. Wright: Numerical Optimization. Springer, 2006.

[45] M. Cavazzuti: Optimization Methods, From Theory to Design. Springer, 2013.

[46] K. F. Man, K. S. Tang, S. Kwong: Genetic Algorithms, Concepts and Design. Springer, 1999.

[47] P. Bangert: Attitude Determination System of UWE-3. Master Thesis, Julius Maximilians University of Würzburg, Würzburg, Germany, 2012.

[48] S. Ghuffar: Design and Implementation of an Attitude Determination Algorithm for the CubeSat UWE-3. Master Thesis, Julius Maximilians University of Würzburg, Würzburg, Germany, 2009.

[49] M. Schmidt, K. Ravandoor, O. Kurz, S. Busch, K. Schilling: Attitude Determination for the Pico-Satellite UWE-2. In: Proceedings in 17th IFAC World Congress, Seoul, Korea, 2008.

[50] V. Grigore: Unscented Kalman Filters for Attitude and Orbit Estimation of a Low Earth Orbit CubeSat. Master Thesis, KTH, Stockholm, Sweden, 2014.

[51] J. Zhou: Design of an INS-GPS Navigation System. Project Report, Unmanned Solutions SL, Madrid, Spain, 2015.

[52] S. Kukreti, A. Walker, P. Putman, K. Cohen: Genetic Algorithm Based LQR for Attitude Control of a Magnetically Actuated CubeSat. In: Proceedings in the 2015 AIAA Infotech @ Aerospace Conference, AIAA 2015-0886, Kissimmee, USA, 2015.

[53] J. Lv, G. Ma, D. Gao: Bias Momentum Satellite Magnetic Attitude Control Based on Genetic Algorithms. In: Proceedings in the 2006 UKACC International Conference on Control, Glasgow, UK, 2006.

[54] S. M. H. Taherzadeh, M. Fatehi, M. Nosratollahi, A. Adami: Optimizing the Satellite Control Gains with Nonlinear Motion Equations using SQP Method. In: International Journal of Computer Applications 118.22, 2015, p. 33-36.